HDW

Search for W pair production in $p\bar{p}$ collisions at $\sqrt{s} = 1.8$ TeV

A Dissertation Presented

by

Hossein Johari

to

The Graduate School

in Partial Fulfillment of the Requirements

for the Degree of

Doctor of Philosophy

in

Physics

Northeastern University
Boston, Massachusetts

April 1995

NORTHEASTERN UNIVERSITY
Graduate School of Arts and Sciences

Dissertation Title: Search for W pair production in $p\bar{p}$ collisions at $\sqrt{s} = 1.8$ TeV

Author: Hossein Johari

Department: Physics

Approved for Dissertation Requirements of Doctor of Philosophy Degree

Takahiro Yasuda 4/25/95
S. Reucroft. 4/25/95.
Michael T. Vaughn 4/25/95

Thesis Committee Date

Paul M. Champion 4/26/95

Head of Department Date

Graduate School Notified of Acceptance

Dean 1 May 95

Date

Search for W pair production in $p\bar{p}$ collisions at $\sqrt{s} = 1.8$ TeV

A Dissertation Presented

by

Hossein Johari

to

The Graduate School

in Partial Fulfillment of the Requirements

for the Degree of

Doctor of Philosophy

in

Physics

Northeastern University
Boston, Massachusetts

April 1995

Acknowledgements

I would like to thank Takahiro Yasuda for introducing me to experimental high energy physics and for his tolerant and continuous support as my thesis advisor. It is a pleasure to work with Taka. His insight in physics is unbelievable and his years of experience made him invaluable. Besides his professional life, he was an older brother to me. I have been so grateful to have Taka as my thesis advisor.

I would like to thank my colleagues at Northeastern University, especially Professor Steve Reucroft for his support through my student's years at Northeastern. I also like to thank my colleagues at the D0 experiment, upgrade group, WZ group and diboson group. I would like to have special thanks to Marcel Demarteau, Hiro Aihara and Darien Wood for their support and Tony Spadafora, Tom Diehl, Nobu Oshima, Brajesh Choudhary, Steven Glenn, Greg Landsberg and Liang-Ping Chen for teaching me different techniques. I would like to thank Jim Cochran who spent a lot of his valuable time with me to discuss about a very detailed stuff. Special thanks will go to spokespersons, Paul Grannis and Hugh Montgomery.

This experiment would not have been possible without the cooperation and efforts of the Fermilab staff.

I would like to thank my parents, my brother and my sister for the understanding, support, patience and encouragement they gave me throughout my years as a student.

Contents

List of Tables

List of Figures

Chapter 1

Introduction

The Standard Model (SM) of electroweak interactions has been extremely successful in the past. The SM had predicted the massive gauge bosons $W^{\pm}$ and Z^0 which mediate the weak nuclear force and the neutral currents as its consequence. The existence of neutral currents was verified in a bubble-chamber experiment at CERN in 1973 [1]. In 1983, the production and decay of the $W^{\pm}$ gauge boson [2] and Z^0 [3] in the leptonic modes were observed at CERN ($\sqrt{s}$ = 540 GeV). Over the last five years, experiments at the LEP e^+e^- collider (CERN) running at the Z^0 peak have performed precise measurement of the SM parameters. The most important tests of the SM at LEP come from the lineshape parameters (M_Z, Γ, σ_h^0), leptonic and hadronic branching ratios, leptonic forward-backward asymmetries, τ polarization measurements, and branching ratios and asymmetries for heavy flavor events. All LEP measurements can be predicted based on the SM at tree level in terms of a single parameter (M_Z or $\sin^2\theta_W$) with small correction terms due to the mass of the top quark in loop diagrams. The precision of the LEP measurements allows us to predict the mass of the top quark to be 178 ± 22 [4] which agrees very well with the recent results from DØ and CDF collaborations [5] at Fermilab on the observation and mass determination of the top quark. These successes make it even more imperative to test additional processes for possible discrepancies between the SM predictions and experimental measurements. One of the aspects of the SM that has not been tested experimentally is the gauge boson self-interaction. The coupling strengths of the gauge boson self-interaction can be measured using the gauge boson pair production processes. This thesis describes a search for W boson pair production events in $p\bar{p}$ collisions at $\sqrt{s} = 1.8$ TeV. The limits on the cross section of W boson pair production and on the triple gauge boson coupling parameters are reported.

This thesis is organized as follows. The theoretical and experimental background of W pair production is described in this chapter. Chapter 2 is devoted to the experimental apparatus, Chapter 3 describes the data analysis, and Chapter 4 contains the conclusions and discussions.

1.1 Theoretical Overview

High-energy physics is the science of the ultimate constituents of matter and the nature of the interactions between them. Experimental research in this field is carried out with giant and expensive particle accelerators to achieve very high energies. One needs to reach the very high energy because many of the fundamental particles have large masses and require a large amount of energy to create them. To study the very small scales of distance associated with elementary particles, one needs the smallest possible wavelength which also means the highest possible energy. According to recent theories, the universe has begun with a "Big Bang" and started to expand since then. Therefore, what we see today including particles and their interactions is the remains of the Big Bang. Based on these theories all interactions were unified in the Big Bang.

In other words, in the very beginning there was only one single force. However, as the universe expands and moves to lower energy (cooling down) this symmetry is badly broken and that is the reason why there are four different forces in nature; the strong nuclear force, the electromagnetic force, the weak nuclear force, and the gravitational force. The SM unifies two of these forces, the electromagnetic, and the weak nuclear forces and explains how the symmetry is broken.

Based on this view, our knowledge of particle physics can be summarized as follows:

- All matter is composed of leptons and quarks. There are three types of charged and neutral leptons. The charged leptons are electron, muon, and tau which have charge e, mass, and spin 1/2. Three neutral leptons with spin 1/2 are almost massless and called neutrino $(\nu_e, \nu_\mu, \nu_\tau)$. Atoms are made of electrons, protons and neutrons. Protons and neutrons are composed of quarks. Six different quarks have been identified; up, down, strange, charm, bottom, and top. Quarks have spin 1/2 and fractional electric charge of proton (2/3 e for up, charm, and top and -1/3 e for down, strange, and bottom). But they have not been observed as free particles. Quarks have color charge which is analogous to the electric charge. There are three types of color charge (red, green, and blue).
- Force is the manifestation of interaction between particles. A matter-field is associated to each of the particles. Interaction between the matter-fields occurs by exchanging various fundamental bosons (integral spin) or a gauge-field. The electromagnetic interaction is a non-nuclear interaction with the longest range and leads to bound states of atoms and molecules. The gauge-field associated to electromagnetic force is the photon. The weak interaction is a short range

process and responsible for β-decays. The weakness of the weak interaction is pictured to their short-range nature via mediation of gauge-fields $W^{\pm}$ and Z^0 with masses of the order of 100 proton masses. The strong interaction is also a short range interaction and responsible for bonding quarks into the protons and neutrons. The gauge-field for strong interactions is the gluon. Color is the gluon charge. Gluons interact not only with quarks but also with themselves via color exchange.

1.2 Standard Model

The strength of a force or interaction between particles is characterized by a coupling constant. In the electromagnetic interaction the coupling constant between charged particles and photons is the dimensionless fine-structure constant $\alpha = \frac{1}{137.0360}$ [4] which determines the magnitude of the fine structure (spin-orbit splitting) in atomic spectra.

Weak interaction occurs between all quarks and leptons. The signature of the weak interaction involves either neutrinos or quarks with a flavor change. The classical example of this force is neutron β-decay.

$$n \rightarrow p + e^- + \bar{\nu}_e$$

Fermi had postulated a contact interaction theory which assumes the weak interaction is point like with the strength $G_F \sim 10^{-5} GeV^{-2}$ between four fermions to describe β-decay [4]. The Fermi theory of weak interaction is badly divergent. The following process

$$\nu_\mu + e^- \rightarrow \mu^- + \nu_e$$

shows this divergence clearly. The total cross section for the above process based on Fermi theory is

$$\sigma_{tot} = \frac{4G_F^2 p^{*2}}{\pi}$$

where p^{*2} is CMS momentum $p^{*2} = s/4$. The cross section from wave theory predicts $\sigma_{max} = \pi/(2p^{*2})$. At sufficiently large energy, the Fermi theory predicts a cross section exceeding the wave theory; when $p^* > \pi/(G_F\sqrt{8})^{1/2} \sim 300\ GeV/c$, $\sigma_{tot} > \sigma_{max}$[6]. Wave theory requires the condition that the scattered intensity can not exceed the intensity in any partial wave. This is also called the unitarity limit. This divergence problem comes from the Fermi constant G_F because it has the dimension of an inverse power of the energy. The above issue partially will be resolved by replacing the point like interaction with the idea of transferring intermediate vector bosons, $W^{\pm}$. The effect of the intermediate vector bosons is to introduce a propagator term $(1 + q^2/M_W^2)^{-1}$ into the scattering amplitude which spreads the interaction over the finite range, of order M_W^{-1}, so that σ_{tot} will tend to be a constant value $G_F^2 M_W^2 \pi$ at high energy. The unitarity is still broken, but logarithmically.

The electroweak theory proposed by Glashow, Salam, and Weinberg [7, 8] is a $SU(2) \otimes U(1)$ gauge theory which unifies the weak and electromagnetic interactions. The theory predicts a massive charged gauge boson $W^{\pm}$ as well as its neutral partner Z^0. A spontaneous symmetry breaking is introduced to explain the masses for $W^{\pm}$ and Z^0. This is done with an isospin doublet of scalar Higgs field which generates mass as a result of self-interaction [9].

The electroweak Lagrangian is

$$\mathcal{L} = -\frac{1}{4}B_{\mu\nu}^2 - \frac{1}{4}W_{\mu\nu}^{a2} + D_\mu\phi^\dagger D^\mu\phi - V(\phi).$$

The covariant derivative is defined as

$$D_\mu \equiv \partial_\mu - \frac{1}{2} i g_1 B_\mu Y - i g_2 W_\mu^a T^a,$$

where Y is the hypercharge generator and T^a is the SU(2) generator. The potential for the scalar Higgs is

$$V(\phi) = \lambda(\phi^\dagger \phi)^2 - \mu^2 \phi^\dagger \phi,$$

where λ is the self-coupling parameter and μ is a mass parameter. The weak mixing angle θ_W is defined by $\tan\theta_W \equiv \frac{g_1}{g_2}$. In a gauge where $\langle\phi\rangle = \sqrt{\frac{1}{2}}(0, v)^T$, the mass term of the gauge bosons in the Lagrangian is

$$\frac{1}{4}\langle\phi^\dagger\rangle(g_1 B_\mu + g_2 W_\mu^a \sigma^a)(g_1 B_\nu + g_2 W_\nu^b \sigma^b)\langle\phi\rangle.$$

Using the mixing angle,

$$\begin{aligned} \begin{pmatrix} A_\mu \\ Z_\mu \end{pmatrix} &\equiv \begin{pmatrix} \cos\theta_W & \sin\theta_W \\ -\sin\theta_W & \cos\theta_W \end{pmatrix} \begin{pmatrix} B_\mu \\ W_\mu^3 \end{pmatrix}, \\ W_\mu &\equiv \sqrt{\frac{1}{2}}(W_\mu^1 + i W_\mu^2), \end{aligned}$$

this expression becomes

$$M_W^2 W_\mu^\dagger W^\mu + \frac{1}{2} M_Z^2 Z_\mu^2,$$

where $M_W^2 \equiv \frac{1}{4} g_2^2 v^2$ and $M_Z^2 \equiv M_W^2/\cos^2\theta_W$. The electromagnetic field A_μ remains massless and couples with

$$e \equiv \frac{g_1 g_2}{\sqrt{g_1^2 + g_2^2}} = g_1 \cos\theta_W.$$

The covariant derivative is now written as

$$D_\mu = \partial_\mu + ieA^\mu Q + \frac{ie}{\sin\theta_W \, \cos\theta_W} Z^\mu (T^3 - Q\sin^2\theta_W)$$

using the weak mixing relationship and $Q = T^3 + Y/2$. The neutral current couplings are obtained from the Z_μ part of the covariant derivative as

$$\begin{aligned} c_L^f &= T^3 - Q\sin^2\theta_W \\ c_R^f &= -Q\sin^2\theta_W \end{aligned}$$

The three generations of leptons, associated with the electron, muon, and tau are grouped as the left-handed SU(2) weak isospin doublets and right-handed singlets as follows:

$$\begin{pmatrix} t_3 = +1/2 \\ \\ t_3 = -1/2 \end{pmatrix}_L \rightarrow \begin{pmatrix} \nu_e \\ \\ e \end{pmatrix}_L \begin{pmatrix} \nu_\mu \\ \\ \mu \end{pmatrix}_L \begin{pmatrix} \nu_\tau \\ \\ \tau \end{pmatrix}_L ,$$

$$\begin{pmatrix} t = 0 \\ \\ t_3 = 0 \end{pmatrix}_R \rightarrow \begin{pmatrix} e \end{pmatrix}_R \begin{pmatrix} \mu \end{pmatrix}_R \begin{pmatrix} \tau \end{pmatrix}_R ,$$

where L and R indicate left-handed and right-handed components. Because of the vector and axial nature of weak interaction, only the left-handed part can be set into doublet weak isospin.

The corresponding sequence of generation for quarks is

$$\begin{pmatrix} u \\ \\ d \end{pmatrix}_L \begin{pmatrix} c \\ \\ s \end{pmatrix}_L \begin{pmatrix} t \\ \\ b \end{pmatrix}_L ,$$

$$\begin{pmatrix} u \end{pmatrix}_R \begin{pmatrix} d \end{pmatrix}_R \begin{pmatrix} c \end{pmatrix}_R ; \begin{pmatrix} s \end{pmatrix}_R \begin{pmatrix} t \end{pmatrix}_R \begin{pmatrix} b \end{pmatrix}_R .$$

Based on the detailed experimental comparison of the hadronic strangeness-conserving and violating weak decays with the muon β decay, Cabibbo postulated that the strength of hadronic weak interaction is shared between the $\Delta S = 0$ and $\Delta S = 1$ transition (S is the strangeness quantum number) [10]. In other words, the weak isospin doublet of quarks, such as

$$\begin{pmatrix} u \\ d \end{pmatrix}_L \text{ should be written as } \begin{pmatrix} u \\ d\ cos\theta_c + s\ sin\theta_c \end{pmatrix}_L$$

where θ_c is the Cabibbo angle, indicating that the amplitudes for $d \rightarrow u$ and $s \rightarrow u$ must be modified by the mixing parameters $\cos\theta_c$ and $\sin\theta_c$. The idea of the transition matrix was generalized to include the third generation of quarks in order to explain CP violation. This matrix is now called the Cabibbo-Kobayashi-Maskawa [11] matrix and is written as follows:

$$J_\mu^{ch} \propto \begin{pmatrix} d & s & b \end{pmatrix}_L \gamma_\mu \mathbf{C} \begin{pmatrix} u \\ c \\ t \end{pmatrix}_L$$

1.3 *W* Pair Production

In the previous section, it was shown that the introduction of the gauge boson $W^{\pm}$ solves partially the unitarity violation at the tree level for the process $\nu_{\mu} + e^{-} \rightarrow \mu^{-} + \nu_{e}$. As it turned out, there are processes that violate unitarity even at the tree level if only the existence of charged gauge bosons is assumed. The process is the gauge boson pair production. The SM solves this problem elegantly. The unitarity violating amplitudes are cancelled by the amplitudes that involve both charged and neutral gauge bosons.

Feynman diagrams for the W pair production in $p\bar{p}$ collisions are shown in Figure 1.1 . The gauge boson self-interaction ($WW\gamma$ and WWZ vertices) is a consequence of the non-Abelian $SU(2) \otimes U(1)$ symmetry of the SM. The cancellations among diagrams take place only if the coupling constants are the exact SM values. If the couplings differ from the SM values due to physics beyond the SM, the cancellations are no longer exact and the cross section of this process will rise as energy.

The gauge boson self-interaction part of the SM Lagrangian becomes

$$\begin{aligned} i\mathcal{L}_{WWV} = g_2\{\sin\theta_W[(A^{\nu}W^{\mu} - A^{\mu}W^{\nu})\partial_{\mu}W^{\dagger}_{\nu} - (A^{\nu}W^{\dagger\mu} - A^{\mu}W^{\dagger\nu})\partial_{\mu}W_{\nu} \\ +(\partial^{\mu}A^{\nu} - \partial^{\nu}A^{\mu})W_{\mu}W^{\dagger}_{\nu}] + \cos\theta_W[A \rightarrow Z]\} \end{aligned}$$

after a lengthy manipulation. Substituting $g_2\sin\theta_W = g_1\cos\theta_W = e$, $g_2\cos\theta_W = e\cot\theta_W$, $W_{\mu\nu} = \partial_{\mu}W_{\nu} - \partial_{\nu}W_{\mu}$, and $A_{\mu\nu} = \partial_{\mu}A_{\nu} - \partial_{\nu}A_{\mu}$, $\mathcal{L}_{WWV}$ is simplified as

$$i\mathcal{L}_{WWV} = e\{W^{\dagger}_{\mu\nu}W^{\mu}A^{\nu} - W^{\dagger\mu}A^{\nu}W_{\mu\nu} + W_{\mu}W^{\dagger}_{\nu}A^{\mu\nu} + \cot\theta_W[A \rightarrow Z]\}$$

A generalized Lagrangian has been developed to describe the $WW\gamma$ and WWZ interactions. The general effective Lorentz invariant Lagrangian is written as

$$i\mathcal{L}^{eff}_{WWV} = g_{WW\gamma}[(g_1^\gamma(W^\dagger_{\mu\nu}W^\mu - W^{\dagger\mu}W_{\mu\nu})A^\nu + \kappa_\gamma W^\dagger_\mu W_\nu A^{\mu\nu} + \frac{\lambda_\gamma}{m_W^2} W^\dagger_{\rho\mu} W^\mu_\nu A_{\nu\rho}] + \cdots + g_{WWZ}[A \to Z] \tag{1.1}$$

where the overall coupling constants are defined as $g_{WW\gamma} = e$ and $g_{WWZ} = e\cot\theta_W$ [12, 13, 14, 15].

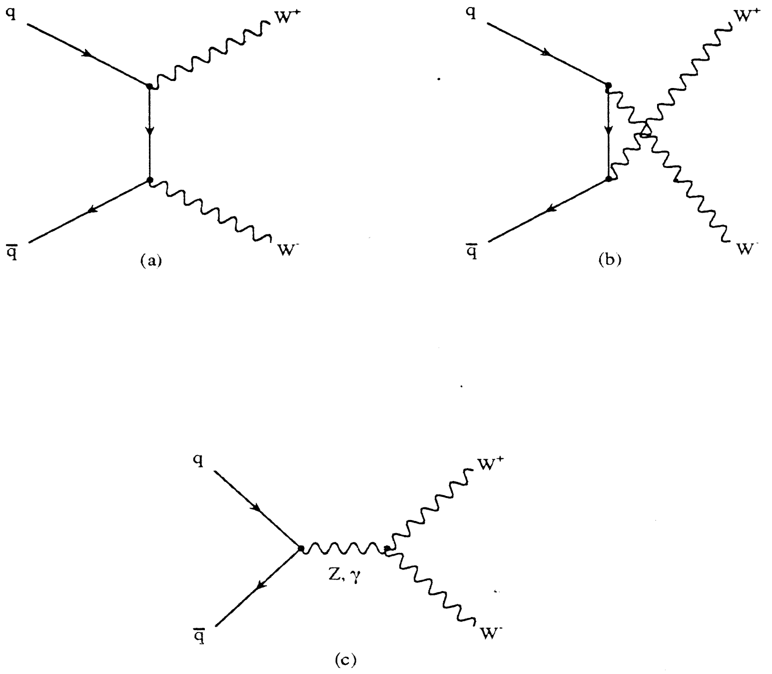

Figure 1.1: The tree-level Feynman diagrams of $q\bar{q} \to W^+W^-$ process.

The Lagrangian contains six coupling parameters after imposing C, P, and CP symmetry: g_1^V, κ_V, and λ_V, where $V = \gamma, Z$ denotes the coupling to the photon or Z^0 boson. g_1^Z is assumed to be equal to g_1^γ, which is restricted to unity by electromagnetic gauge invariance. The effective Lagrangian can be reduced to the SM Lagrangian by setting $\kappa_V = 1$ ($\Delta\kappa_V \equiv \kappa_V - 1 = 0$) and $\lambda_V = 0$. The $WW\gamma$ couplings are related to the magnetic dipole (μ_W) and electric quadrupole (Q^e_W) moments of the W boson:

$$\mu_W = \frac{e}{2m_W}(1 + \kappa_\gamma + \lambda_\gamma)$$

$$Q_W = -\frac{e}{m^2_W}(\kappa_\gamma - \lambda_\gamma)$$

[15, 16], where e and m_W are the charge and the mass of the W boson.

This effective Lagrangian leads to a cross section which grows with $\hat{s}$ for non-SM values of the couplings. In order to avoid unitarity violation, the anomalous couplings are parameterized as form factors with a scale, Λ, (e.g. $\lambda/(1 + \hat{s}/\Lambda^2)^2$). Figure 1.2 shows how the cross section behaves with different scales, Λ, as a function of the coupling parameter λ. By requiring that tree-level unitarity is satisfied, a constraint on κ and λ

$$\Lambda \leq \left(\frac{6.88}{(\kappa-1)^2+2\lambda^2}\right)^{1/4} \text{ TeV}$$

is obtained [16].

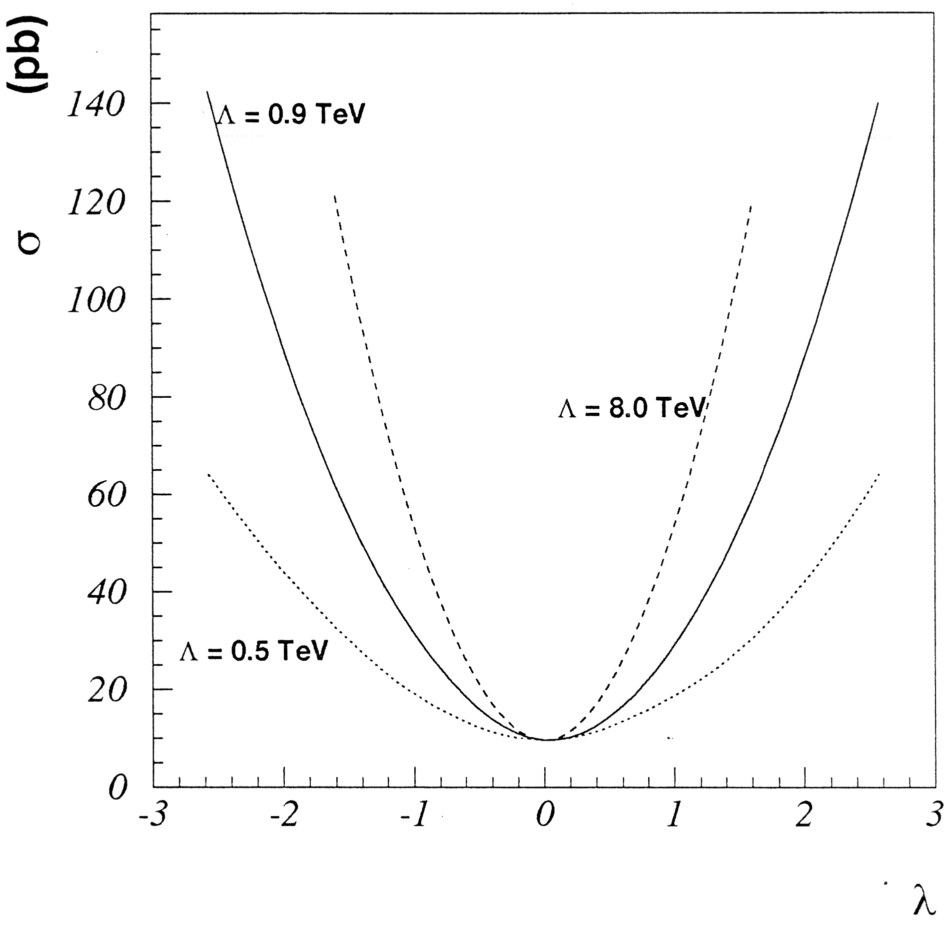

Figure 1.2: W pair cross section (pb) as a function of λ ($\Delta\kappa = 0$), for $\Lambda =$ 500 GeV (dotted line), 900 GeV (solid line), and 8 TeV (dashed line).

1.4 Cross Section Calculation for W Pair Production

A high-energy proton beam may usefully be regarded as an unseparated, broad-band beam of quarks, antiquarks and gluons. For hard scattering phenomena that are the principal interest here, it is the rate of encounters among energetic constituents that determines interaction rates. Since the essence of the parton model is to regard a high-energy proton as a collection of quasi-free partons which share its momentum, we envisage a proton of momentum P as being made of partons carrying longitudinal momenta x_iP, where the momentum fractions x_i satisfy $0 \leq x_i \leq 1$ and $\sum_i x_i = 1$.

The cross section for the following hadronic reaction (in the spirit of the parton model)

$$a + b \rightarrow c + d + \text{anything} \tag{1.2}$$

is given by

$$d\sigma = \sum_{partons}^{ij} f_i^a(x_a) f_j^b(x_b) d\hat{\sigma}(i + j \rightarrow c + d + X') \tag{1.3}$$

where $f_i^a(x_a)$ is probability of finding constituent i in hadron a with x_iP momentum and $\hat{\sigma}(i + j \rightarrow c + d + X')$ is the cross section for the elementary process leading to the desired final state. The masses of the final state particles are M_c and M_d. If c is produced at a C.M. angle θ with transverse momentum $P_\perp = x_\perp \frac{\sqrt{s}}{2}$, the invariant cross section for the reaction is [17]

$$E\frac{d\sigma}{d^3p} = \frac{1}{\pi}\sum_{i,j}\int_{x_{min}}^{1} \frac{dx_a}{x_a - x_\perp\left[\frac{\chi + cos\theta}{2sin\theta}\right]} x_a x_b f_i^a(x_a) f_j^b(x_b) \frac{d\hat{\sigma}}{d\hat{t}}(\hat{s}, \hat{t}, \hat{u}). \tag{1.4}$$

The elementary parton model as sketched here is an approximation to reality. The most important modification to the elementary picture is due to the strong interaction (QCD) corrections to the parton distributions. In leading logarithmic approximation (Gribov and Lipatov, 1972a, 1972b) these corrections are process independent and can be incorporated by the replacement

$$f_i^a(x_a) \rightarrow f_i^a(x_a, Q^2). \tag{1.5}$$

There is some ambiguity surrounding the choice of scale Q^2 in a particular process. It should be of the order of the subenergy,

$$Q^2 \approx \hat{s}. \tag{1.6}$$

The Feynman diagrams for the process

$$q_i\bar{q}_i \rightarrow W^+W^- \tag{1.7}$$

are shown in Figure 1.1 . The differential cross section for the elementary process [12] , averaged over quark colors, is written as

$$\begin{aligned}
\frac{d\sigma}{dz} &= \frac{\hat{s}\beta_W}{2}\frac{d\sigma}{d\hat{t}} \\
&= \frac{\pi\alpha^2\beta_W}{24x_W^2\hat{s}}([\frac{\hat{u}\hat{t}-M_W^4}{\hat{s}^2}][3-[\frac{\hat{s}-6M_W^2}{\hat{s}-M_Z^2}]\frac{c_L^i}{\tau_{3i}(1-x_w)}+[\frac{\hat{s}}{\hat{s}-M_Z^2}]^2 \\
&\quad [\beta_W^2+\frac{12M_W^4}{\hat{s}^2}][\frac{{c_L^i}^2+{c_R^i}^2}{(1-x_W)^2}]] \\
&\quad -4[\frac{M_Z^2}{\hat{s}-M_Z^2}]\frac{c_L^i}{\tau_{3i}}+4\frac{M_Z^2\hat{s}\beta_W^2}{(\hat{s}-M_Z^2)^2}[\frac{{c_L^i}^2+{c_R^i}^2}{1-x_W}] \\
&\quad +\Theta(-e_i)[2[1+\frac{M_Z^2}{\hat{s}-M_Z^2}\frac{c_L^i}{\tau_{3i}}][\frac{\hat{u}\hat{t}-M_W^4}{\hat{s}\hat{t}}-\frac{2M_W^2}{\hat{t}}]+\frac{\hat{u}\hat{t}-M_W^4}{\hat{t}^2}] \\
&\quad +\Theta(e_i)[2[1+\frac{M_Z^2}{\hat{s}-M_Z^2}\frac{c_L^i}{\tau_{3i}}][\frac{\hat{u}\hat{t}-M_W^4}{\hat{s}\hat{u}}-\frac{2M_W^2}{\hat{u}}]+\frac{\hat{u}\hat{t}-M_W^4}{\hat{u}^2}])
\end{aligned} \tag{1.8}$$

decays to dilepton (ee, eμ, $\mu\mu$) channels in $p\bar{p}$ collisions at $\sqrt{s} = 1.8$ TeV. The experiment was carried out with the D0 detector at Fermilab (Fermi National Accelerator Laboratory, Batavia, IL) between August 1992 and May 1993. The data sample corresponds to an integrated luminosity of 14 pb^{-1}. From the number of observed signal events and estimated background events, the 95% confidence level upper limit on the W boson pair production cross section is obtained. Limits on the coupling parameters, λ and $\Delta\kappa$, are also set, assuming $\lambda_\gamma = \lambda_Z$ and $\kappa_\gamma = \kappa_Z$.

Chapter 2

Experimental Apparatus

2.1 The Accelerator

The Tevatron collider at Fermilab is a proton–antiproton colliding beam machine with a center of mass energy of 1.8 TeV which is the highest in the world. The Tevatron collider is a very complicated device and actually consists of seven separate parts (Figure 2.1)

- A Cockroft-Walton Accelerator
- The Linac
- The Booster Synchrotron
- The Main Ring
- The Target Hall
- The Antiproton Source
- The Tevatron Ring

The process begins with H^- ions which are obtained by ionizing hydrogen gas with electrons. These ions are accelerated in the Cockroft-Walton accelerator which produces a static electric field of about 750 keV. The ions are then injected into the 150 meter long Linac. This device induces an oscillating electric field between a series of electrodes. The ions are accelerated by the electric field whose oscillation is synchronized to the passage of ions through the electrodes. The electrons from the H^- ions are stripped off by passing through a carbon foil. The protons are then steered into the Booster synchrotron ring which is a cyclic machine with 500 meters in circumference. In the synchrotron ring the particles are confined to a closed orbit by a series of bending magnets. On each pass around the ring the particle's energy is increased by acceleration in a synchronized rf cavity. As the momentum increases, the magnetic field in the bending magnets must be increased to keep particles inside the ring. In this stage the protons are accelerated to 8 GeV and injected into the main ring with 3.7 miles in circumference. While circulating in the main ring, protons are accelerated to 120 GeV and formed into a set of bunches with 2×10^{12} protons per bunch. To make antiprotons these bunches are then extracted onto a nickel/copper target, producing 2×10^7 antiprotons per proton bunch.

Because the created antiprotons have a broad energy spectrum and wide angular divergence, they are initially focused by a lithium magnetic lens and injected into the first of two antiproton storage rings, the Debuncher. In this storage ring the antiproton energies are equalized and formed into a compact and coherent beam. This process is known as cooling. Two steps have to be taken for a coherent beam. The first step is debunching which uses computer controlled radio-frequency pulses to smooth the antiprotons into a uniform ring (all the particles have approximately the

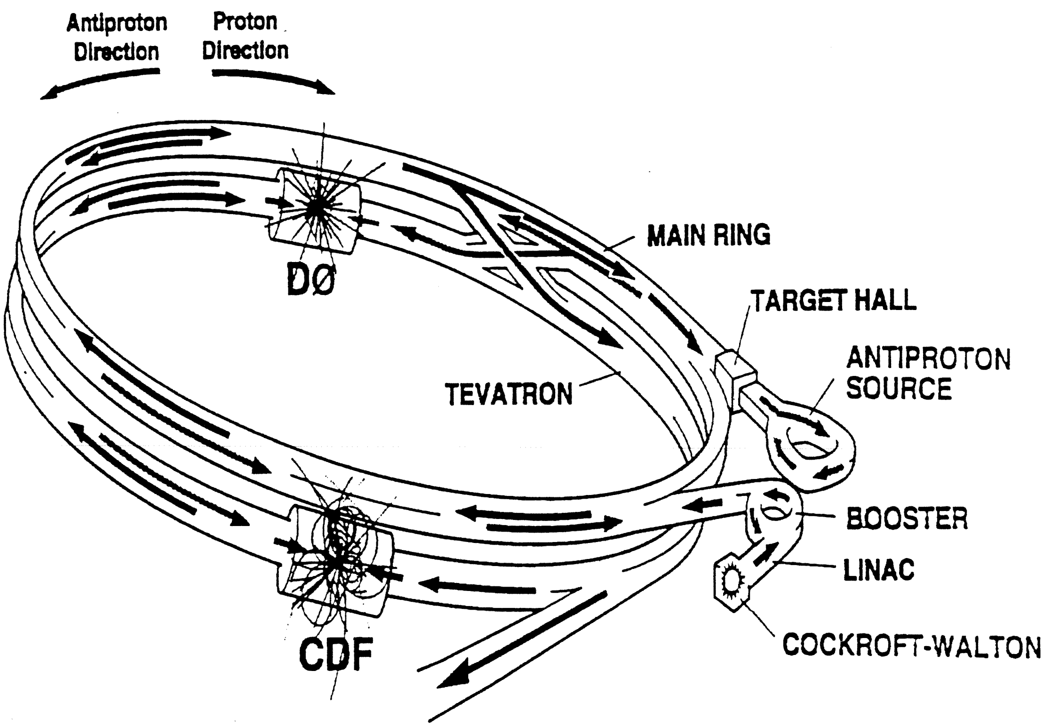

Figure 2.1: The schematic layout of Tevatron accelerator complex.

same momentum). The second step is stochastic cooling which squeezes this ring in the transverse plane by using beam sensors. The beam sensors transmit information about the beam profile to kicker electrodes which introduce corrective magnetic fields.

The cooling processes run continuously and prepare a monochromatic squeezed antiproton beam with 2×10^6 antiprotons for the second antiproton storage ring, the Accumulator. When about 4×10^{11} antiprotons are stored in the Accumulator which takes 8 to 12 hours, the antiprotons are transferred to the main ring, accelerated to 150 GeV and then injected into the Tevatron, traveling in the opposite direction to the protons.

The Tevatron is in the same tunnel as the main ring but uses superconducting magnets which operate at a temperature of 4.7 K and create a field of 4 Tesla to achieve a much higher energy. Finally the six bunches of protons with about 10^{11} particles per bunch and six bunches of antiprotons with about 5×10^{10} particles per bunch are simultaneously accelerated to the full energy (0.9 TeV). Once at full energy the beams are squeezed very hard at two beam crossing points B0(CDF) and D0. The interval between beam crossings is 3.5 μsec. The bunch spacing is about 186 RF buckets where each RF bucket corresponds to 18.8 nsec.

The typical lifetime of the Tevatron beams is about 12–18 hours. During this time new antiprotons are stored into the Accumulator for a continuous operation of the Tevatron. The maximum luminosity was 9×10^{30} $cm^{-2}s^{-1}$ during 1992–1993 operation [30]. For head on collisions, the instantaneous luminosity can be calculated with $L = \frac{N_p N_{\bar{p}}}{4\pi\sigma^2}$ where N_p and $N_{\bar{p}}$ are the number of protons and antiprotons per bunch respectively, and σ is the overlap distribution. D0 performs a precise measurement for the luminosity by including the beta functions and measured beam emittances for each proton and antiproton bunches [31]. A cross check for the luminosity is made using MinBias and ZeroBias events and also appropriate corrections related with the experimental dead time, multiple interaction, and main ring vetoing are taken into account [31].

2.2 D0 Detector

The D0 Detector has been constructed to study proton-antiproton collisions at $\sqrt{s} = 1.8$ TeV in the Fermilab Tevatron Collider [32].

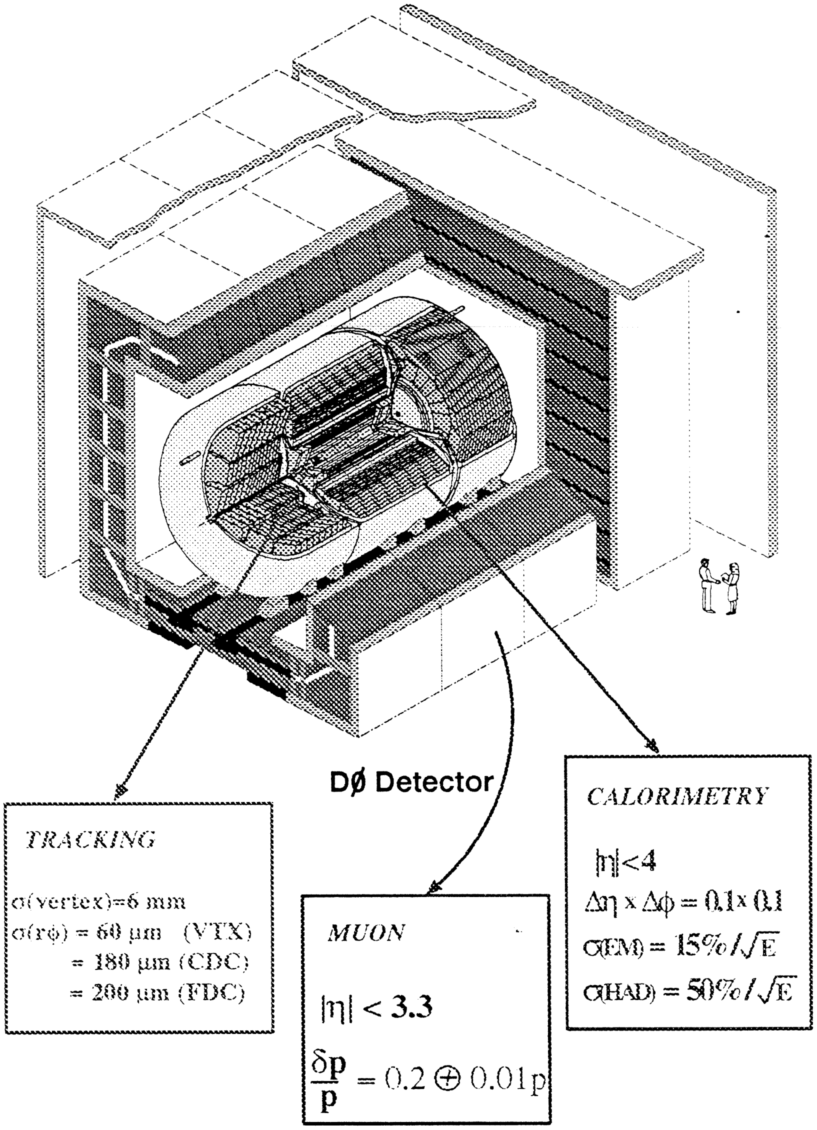

Figure 2.2: DØ detector

The experiment was first provisionally approved in 1983 and the full conceptual design report was prepared a year later. DØ is a multipurpose and second generation detector (UA1, UA2, and CDF are first generation detectors) which was optimized with the following three general goals in mind:

- Excellent identification and measurement of electrons and muons.
- Good measurement of parton jets at large E_T through highly segmented calorimetry with good energy resolution.
- A well-controlled measure of missing transverse energy ($\not{E}_T$) as a means of signalling the presence of neutrinos and other non-interacting particles.

These principles are derived from the observation that new objects or phenomena typically have appreciable branching ratios into states including leptons and jets, while the dominating QCD backgrounds have quite small leptonic branching fractions.

The detector was designed with the following features: stable, unit gain, hermetic, finely segmented, thick and radiation-hard calorimetry, based on the detection of ionization in liquid argon. The inner radius of the calorimetry was chosen to be small to accommodate the desired depth and not compromise the surrounding muon detector; muon detection with a thick magnetized iron absorber to provide sufficient momentum measurement and to minimize backgrounds from hadron punchthrough, and finally a compact non-magnetic tracking volume within r = 75 cm with adequate spatial resolution and particular emphasis on the suppression of backgrounds to electrons. Figure 2.2 shows an isometric view of the detector. A right-handed coordinate system is adapted, in which the z-axis is along the proton direction and the y-axis is upward. The angles ϕ and θ are respectively the azimuthal and polar angles (θ

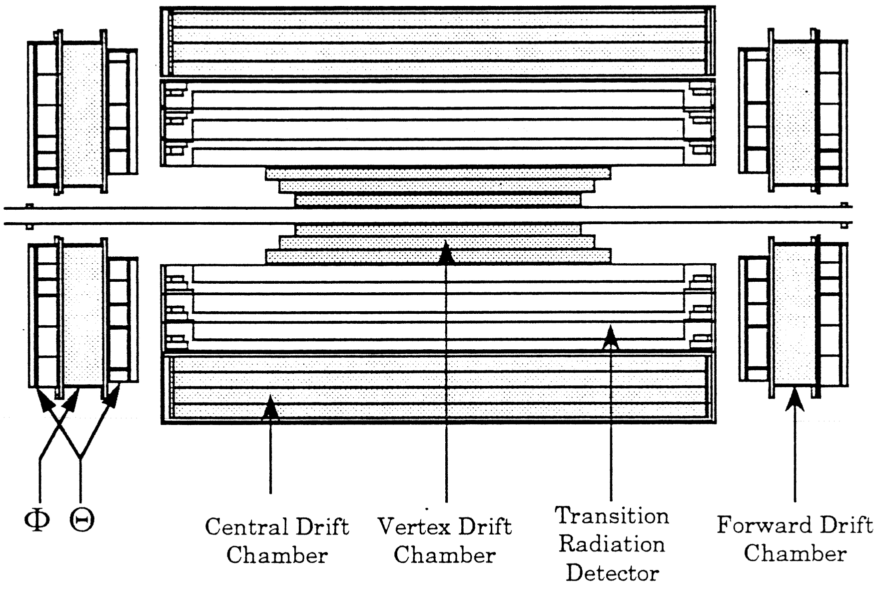

Figure 2.3: Central Detectors

= 0 along the proton beam direction). The r-coordinate denotes the perpendicular distance from the beam axes. The pseudo-rapidity, $\eta = -ln(tan(\theta/2))$, approximates the true rapidity for finite angles in the limit that $(m/E) \rightarrow 0$.

2.2.1 Central Detector (CD)

In order to identify electrons and muons it is imperative to reconstruct the tracks of the particles. On the other hand, track information like dE/dx and track multiplicity is used as a confirmation of what is seen in the calorimeter.

The Central Detector is comprised of the following sub-detectors:

- Vertex Drift Chambers (VTX)
- Transition Radiation Detector (TRD)

- Central Drift Chambers (CDC)
- Forward Drift Chambers (FDC)

The VTX, TRD, and CDC are arranged in three cylinders concentric with the beams. The FDCs are oriented perpendicular to the beams. Figure 2.3 shows the CD layout. The full set of CD detectors fit within the inner cylindrical aperture of the calorimeter in a volume bounded by r=78 cm and z=±135 cm. The DØ central tracking system does not have a central magnetic field. Therefore, without measuring momenta of charged particles, the prime considerations for tracking are good two-track resolving power, high efficiency, and good ionization energy measurement so as to distinguish single electrons from closed-spaced conversion pairs. The TRD is included in order to gain an additional rejection of isolated pions beyond that given by the calorimeter alone.

Vertex Drift Chambers (VTX)

The VTX was designed to identify secondary vertices from c and b quark decays. An additional design goal of the vertex chamber is to complement the other tracking detectors in track reconstruction, dE/dx measurement and vertex finding.

The VTX chamber is the innermost tracking detector in DØ. It has an inner radius of 3.7 cm (just outside the beryllium beam pipe) and an outer active radius of r=16.2 cm. There are three mechanically-independent concentric layers of cells in the VTX chamber. In each cell, eight sense wires provide measurement of the r-ϕ coordinate. The innermost layer (VTX0) has 16 cells in azimuth with length 97 cm; the outer two layers (VTX1, VTX2) have 32 cells with length of 107 and 117 cm, respectively. To resolve left-right ambiguities, adjacent sense wires are staggered by ±100 μm and to further aid pattern recognition the cells of the three layers are offset in ϕ. A spatial resolution of 60 μm for drift distances greater than 2 mm was measured for the vertex detector. The track pair resolution efficiency was measured to be better than 90% for separation greater than 0.63 mm.

Transition Radiation Detector (TRD)

This device has not been used in this analysis but it shows promise for providing particle identification at high energies. A charged particle emits transition radiation when it crosses the interface between media with different dielectric or magnetic properties. When the particle is in the region of low dielectric constant, polarization effects in the surrounding medium are small, and the electric field associated with the moving charge has a large spatial extent. However, when the particle crosses the interface to the region of higher dielectric constant, polarization effects are larger, thereby reducing the extent of the electric field in the medium. The sudden redistribution of charges in the medium associated with the changing electric field of the particle gives rise to the transition radiation. At high energy, transition radiation is primarily emitted as X-rays. The D0 TRD is a three layer device which fills the gap between the VTX and CDC. Each layer has 393 layers of 18 μm polyethylene foil with a mean separation of 150 μm. After each section of radiator, a drift chamber collects the electrons produced by photoelectric absorption of the transition radiation X-rays. Xenon gas is employed because of its ready ionization by X-rays. For D0 the X-rays have an energy distribution which peaks at 8 KeV.

Electrons are the only charged particles to be produced with sufficient energy at the Tevatron to induce detectable transition radiation. The TRD can be used to confirm the isolated electrons. The TRD has shown a factor of ten rejection against pions.

Central Drift Chambers (CDC)

The Central Drift Chamber provides track information on isolated charged particle. The CDC is located after the TRD and just prior to the Central Calorimeter. It consists of four concentric rings of 32 azimuthal cells per ring and each cell contains seven 30 μm gold-plated tungsten sense wires. The rϕ measurements rely on the anode wires of the CDC which run parallel to the beam direction. The z position of a track point is measured twice in each layer with delay lines in the modules and outside the sense wire plane. The delay lines are made of carbon fiber rods covered with one winding magnet wire. Signals are induced on the delay lines by avalanche on the nearest sense wires and propagate along the line at 2.4 mm/ns, then read out at each end. The spatial resolutions were measured to be 2 mm along the length of the detector (z) and 150 μm in the rϕ plane. Table 2.1 shows some basic information about the CDC detector.

FDC

The Forward Drift Chambers extend the coverage for charged particle tracking down to $\theta \approx 5^\circ$ with respect to the beams. These chambers are located at either end of the concentric barrels of the VTX, TRD, and CDC and just before the entrance wall of the end calorimeter. The FDC consists of three separate chambers: the Φ module whose sense wires are radial and measure the ϕ coordinate sandwiched between a pair of Θ modules whose sense wires measure the θ coordinate.

Radius (4 layers)	$R_{in} = 49.5cm$; $R_{out} = 74.5cm$
Length	$180cm$
Sector	32
Sense Wires	7 per cell; 896 total
Sense Wire Separation	6.0 mm radially with 200 μm stagger
Delay Lines	2 per cell; 256 total
Gas	Ar 93%; CH4 4%; CO_2 3%; H_2O 0.5%
Average Drift Field	620 V/cm
Average Drift Velocity	34 μm/nsec
Maximum Drift Distance	7 cm
Position Resolution	$r\phi \sim 150\mu m$; $z \sim 2mm$
Tracking Efficiency	89%

Table 2.1: CDC detector parameters

Each Θ module consists of four mechanically separate quadrants, each containing six rectangular cells at increasing radii. All the cells have eight anode wires (wire plane in ϕ z) and have one delay line to give a ϕ measurement. Each Φ module is a single chamber containing 36 sectors over the full ϕ range. Each Φ sector consists of 16 anode wires.

The FDC has a drift resolution in rϕ of 180 μm and 2 mm along the delay lines. Table 2.2 shows a more detailed description.

2.2.2 Calorimeter

The calorimeter is crucial for the DØ detector. Since there is no central magnetic field, calorimetry must provide the energy measurement for electrons, photons and jets. In addition, the calorimeter plays important roles in the identification of electrons, photons, jets and muons, and in establishing the transverse energy balance in an event. Figure 2.4 shows the calorimeter system in which a central calorimeter (CC) covers roughly $|\eta| \leq 1$ and a pair of end calorimeters, (ECN (north) and ECS (south)), extends the coverage out to $|\eta| \approx 4$.

There are two basic types of calorimeter used to measure the energy of a particle. One is a total absorption calorimeter. As a particle traverses this type of calorimeter, it loses all its energy in the material and all the energy lost by the particle is seen by the detector. The second type of calorimeter is a sampling calorimeter. A sampling calorimeter samples only a part of the energy lost by a particle. A correction has to be made to convert the fraction of the energy measured to the full energy lost by the particle. This conversion factor is called the sampling factor. A sampling calorimeter is normally composed of a dense absorbing material and a less dense active material.

	Φ	Θ
Radius	11.0 – 61.3 cm	11 – 62 cm
Z extent	113.0 – 127.0 cm	104.8 – 111.2 cm
Sectors	36	4 quadrants of 6 layers
Sense Wires	8 per cell; 288 total	8 per cell; 384 total
Delay Lines	None	1 per cell; 48 total
Average Drift Field	1.0 kV/cm	1.0 kV/cm
Average Drift Velocity	37 μm/nsec	40 μm/nsec
Maximum Drift Distance	5.0 cm	5.0 cm
Position Resolution	$\sim 200\mu$ m	$\sim 300\mu$ m
Tracking Efficiency	85%	85%

Table 2.2: FDC detector parameters

In the less dense material, ionization charge is produced by the particles in the shower traversing through the material. Showers of particles are mostly produced in the absorbing material where most of the initial particle's energy is lost. The calorimeter is designed to produce electronic signals proportional to the deposited energy.

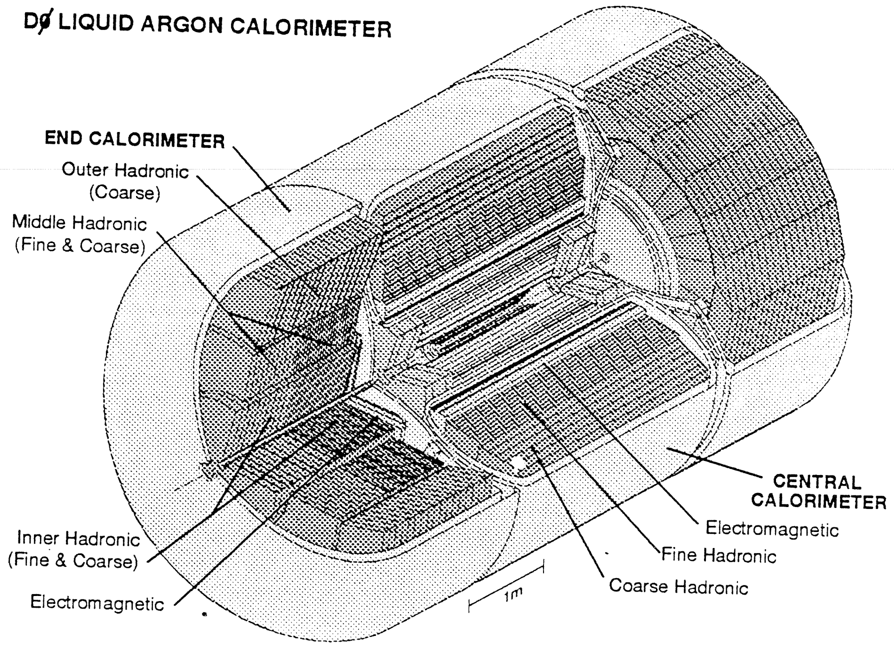

Figure 2.4: DØ Calorimeter system

The DØ calorimeter is a sampling calorimeter. The absorber materials used in the DØ calorimeter are uranium, copper, and stainless steel. The active medium is liquid argon (LAr). The basic structure of the DØ calorimeter is an absorber material between two 2.3 mm LAr gaps on either side of a 1.3 mm thick G10 board. The G10 boards have copper pads inside and are covered with a resistive coating on their outer surfaces. The energy of particles traversing the detector is measured by collecting the charge deposited in LAr gaps. The shower of particles from the interaction of the primary particle ionizes the LAr. The electrons liberated from the LAr drift across the gap (typical drift time is about 450 ns), because an electric field with strength of 8.7 kV/cm is applied between the absorber and the resistive coat, and then induce a pulse on the copper readout pad. Figure 2.5 shows a schematic view of the DØ liquid argon calorimeter unit cell.

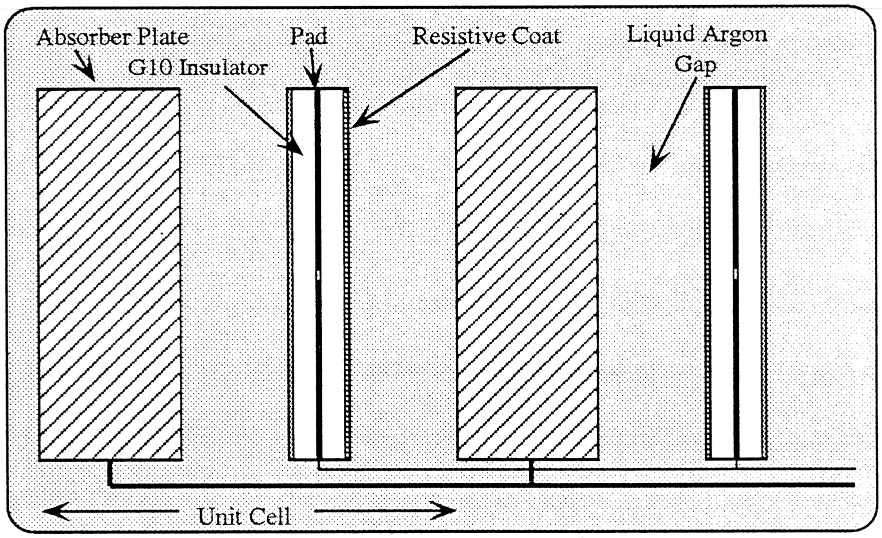

Figure 2.5: The schematic view of the DØ liquid argon calorimeter unit cell.

Central Calorimeter (CC)

The central calorimeter covers the central portion of the detector $|\eta| < 1.2$. The CC is subdivided into three subsystems. These are the electromagnetic calorimeter, the fine hadronic calorimeter, and the coarse hadronic calorimeter. The lateral segmentation of the calorimeter is 0.1×0.1 in $\eta - \phi$ space at all longitudinal depths except the third layer of the electromagnetic calorimeter. The segmentation of this layer is 0.05×0.05 in $\eta - \phi$ space, in order to optimize the position resolution at the shower maximum for electrons and photons. The innermost calorimeter of the CC is the electromagnetic calorimeter (CCEM). Its main purpose is the energy measurement of electromagnetic particles like electrons and photons. This portion forms a cylinder around the beam direction.

The fine hadronic calorimeter is designed to collect the energy deposited by more penetrating particles such as pions. CC fine hadronic (CCFH) forms a cylindrical ring around the EM calorimeter so that both CCFH and CCEM are concentric about the beam direction. The CCFH ring is composed of 16 CCFH modules covering 2π in ϕ. Hadronic particles interact differently in material than EM particles. Nuclear interactions are the major type of interactions through which hadronic particles lose their energy. Since hadronic showers show large fluctuation in the depth of interaction, the DØ calorimeter system has additional calorimetry to provide leakage coverage. In the central region, the CC coarse hadronic calorimeter (CCCH) forms a cylinder just outside of CCFH so that all three calorimeters are concentric around the direction of beam. The CCCH ring consists of 16 modules staggered with the CCFH and no longitudinal cracks between the two rings are aligned. Table 2.3 shows the CC module parameters.

End Calorimeter (EC)

The end calorimeter (EC) covers the pseudorapidity range $1.1 < |\eta| < 4.5$. Similar to the CC, the EC is subdivided in terms of EM, FH, and CH. In the very forward region ($2.0 < |\eta| < 4.5$) the towers pass through Electromagnetic (EM),

	EM	FH	CH
Number of Modules	32	16	16
Absorber	U	UNb	Cu
Absorber Thickness (mm)	3	6	46.5
Argon Gap (mm)	2.3	2.3	2.3
No. of readout boards	21	50	9
Number of readout layers	4	3	1
Cells per readout layer	2,2,7,10	20,16,14	9
Total radiation lengths (X_0)	20.5	96.0	32.9
Total interaction lengths (λ)	0.76	3.2	3.2
Sampling fraction	11.79	6.79	1.45

Table 2.3: CC detector parameters

Inner Fine Hadronic (IFH), and Inner Coarse Hadronic (ICH) layers. In the region $1.5 < |\eta| < 2.0$, the towers pass through EM, IFH, Middle Fine Hadronic (MFH), and Middle Coarse Hadronic (MCH) layers. And finally, in the region $1.0 < |\eta| < 1.5$ the towers pass through MCH and Outer Hadronic (OH) layers. Clearly this leaves something of a *hole* with respect to electron coverage. Table 2.4 shows the module parameters for EC.

Massless gaps and the ICD

The CC/EC transition region, *i.e.*, $0.8 < |\eta| < 1.4$ in the calorimeter contains considerable amount of uninstrumented material. The energy lost in this region is not detected. To correct for the energy loss in the uninstrumented region, the DØ detector calorimeter system includes two different types of detectors.

One is an array of scintillation counter tiles called the intercryostat detector (ICD). An array of ICD modules is mounted on the front surface of each EC cryostat. Each ICD array consists of 384 scintillator tiles of size 0.1×0.1 in $\eta - \phi$ space. These tiles are the same size as the calorimeter cells and form a pseudo-projective structure with the calorimeter cells. The ICD readout uses phototubes.

In addition to the ICD, massless gap modules are mounted on the surfaces of the CCFH, ECMH, and ECOH modules. These modules consist of two signal boards surrounded by three LAr gaps. The size of the readout cells of the massless gaps is 0.1×0.1 in $\eta - \phi$ space. The massless gaps reside inside the calorimeter cryostat.

	EM	IFH	ICH	MFH	MCH	OH
Number of Modules	1	1	1	16	16	16
Absorber	U	UNb	SS	UNb	SS	SS
Absorber Thickness (mm)	4	6	6	6	46.5	46.5
Argon Gap (mm)	0.23	0.21	0.21	0.22	0.22	0.22
No. of readout boards	18	64	12	60	14	24
Number of readout layers	4	4	1	4	1	3
Cells per readout layer	2,2,6,8	16	14	15	12	8
Total radiation lengths (X_0)	20.5	121.8	32.8	115.5	37.9	65.1
Total interaction lengths (λ)	0.95	4.9	3.6	4.0	4.1	7.0
Sampling fraction	11.9	5.7	1.5	6.7	1.6	1.6

Table 2.4: EC detector parameters

2.2.3 The muon system

Muons are identified by their very penetrating nature. They do not interact strongly. The DØ muon system is located outside of the calorimeter system which is 13−18 interaction lengths thick. Muons are momentum analyzed with the ~ 2 T toroidal magnetic field and drift chamber systems.

The DØ muon system is built around five iron toroidal magnets, the CF ($|\eta| < 1.0$), two EF ($1.0 < |\eta| < 2.5$), and two SAMUS, (Small Angle MUon System) toroids ($2.5 < |\eta| < 3.6$). Figure 2.5 a the cross section view of the muon system. Associated with these magnets are several layers of proportional drift tube chambers: one just inside the iron (A layer), one just outside the iron (B layer), and one after an air gap of 1-3 m (C layer). Each of these is divided into sublayers of drift tubes: four for the A layer and three each for the B and C layers. Due to various practical considerations not all regions of $\eta - \phi$ space have full 3 layer coverage. The large number of interaction lengths in the calorimeter and muon toroids provides a very clean environment for the identification and the momentum measurement of high p_T muons over most of the η region. The minimum momentum required for a muon to pass through the calorimeter and iron varies from 3.5 GeV/c at $\eta = 0$ to 5 GeV/c at higher η. The drift resolution is 0.53 mm. Muon system parameters are shown in Table 2.5 .

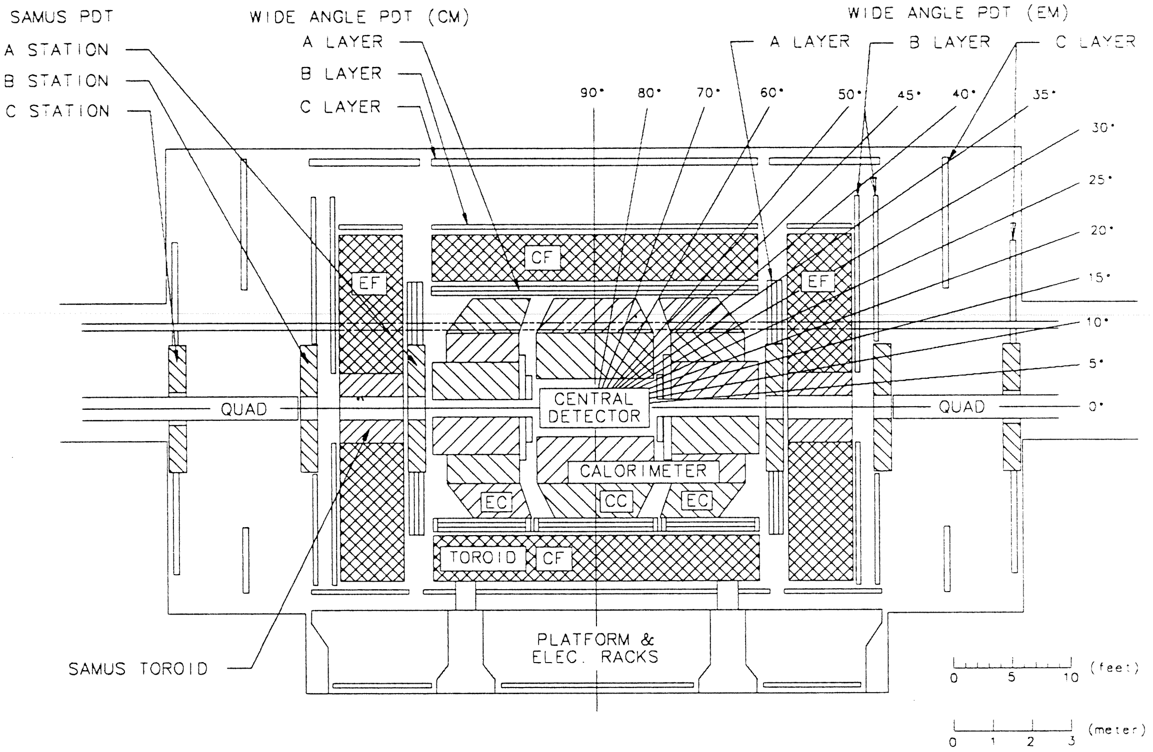

Figure 2.6: The muon system

	WAMUS	SAMUS
Rapidity coverage	$\|\eta\| \leq 1.7$	$1.7 \leq \|\eta\| \leq 3.6$
Magnetic field	2 T	2 T
Number of chambers	164	6
Interaction lengths	13.4	18.7
Bend view resolution	0.53 mm	0.35 mm
Non-bend resolution	3 mm	0.35 mm
Average Drift Velocity	6.5 cm/μs	9.7 cm/μs

Table 2.5: Muon spectrometer system parameters

2.2.4 Trigger and Data Acquisition system

A typical luminosity in DØ is about $5 \times 10^{30} cm^{-2} s^{-1}$. At a center of mass energy of 1.8 TeV the total cross section (elastic plus inelastic) for $p\bar{p} \rightarrow X$ is approximately 70 mb ($= 7 \times 10^{-26} cm^{-2}$). Therefore, the rate of $p\bar{p}$ interactions is 350,000 Hz. The vast majority of these interactions are uninteresting. A multilevel triggering system has been designed to filter out the unwanted events.

There are three different trigger levels in DØ. The Level 0 scintillator-based

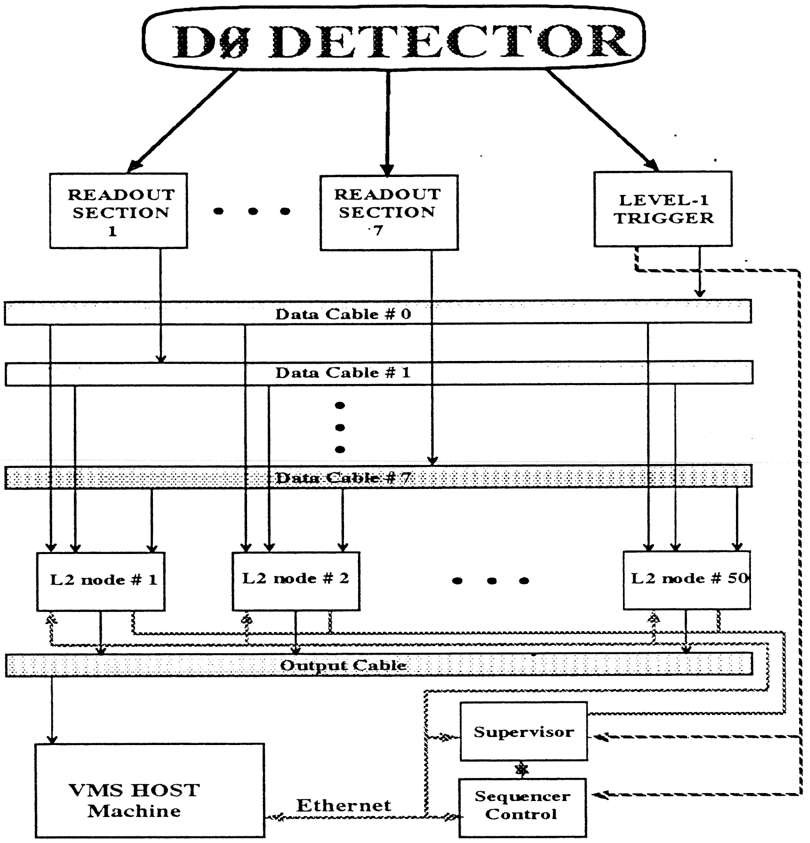

Figure 2.7: The data acquisition system

trigger indicates the occurrence of an inelastic collision. The Level 1 trigger is a collection of hardware trigger elements arranged in a flexible and easily modified software-driven architecture. The Level 1 trigger is based on the transverse energy in the calorimeter and aligned hits in the muon system. Most Level 1 triggers operate within the 3.5 μs time interval between bunch crossings. Others, however, require several bunch crossing intervals to complete computations and are referred to as Level 1.5 triggers. Once an event is passed by the Level 1 or Level 1.5 trigger, it is sent through the standard DØ data acquisition pathway to a farm of microprocessors which serve as event builders as well as the Level 2 software trigger system. The

Level 2 triggers use sophisticated algorithms to reduce the event rate before passing events to the host computers for event monitoring and recording. Figure 2.6 shows a block diagram of the trigger and data acquisition system.

Level 0

The Level 0 consists of two scintillator hodoscopes. Each is mounted on the front surfaces of the opposing EC cryostat (perpendicular to the beam direction). These hodoscopes have two planes of scintillation counters rotated by 90^0. Each hodoscope has 20 short ($7cm \times 7cm$) scintillation elements readout by single photomultiplier tube and 8 long ($7cm \times 65cm$) elements each readout by 2 photomultipliers. These hodoscopes give partial coverage for the pseudorapidity range $1.9 < |\eta| < 4.3$ and nearly complete coverage over $2.2 < |\eta| < 3.9$. The Level 0 trigger registers the presence of inelastic collisions by detecting low angle particles produced in the interaction region.

Level 1 (Hardware trigger)

The Level 1 trigger framework gathers digital information from the Level 0, calorimeter, and muon systems. A decision has to be made before the next beam crossing ($3.5\mu s$) by the Level 1 as to whether a particular event is to be kept for further examination. A total of 32 possible triggers are available. Each is the logical combination of 256 programmable input terms. The calorimeter trigger extends to $|\eta| = 3.2$ in trigger towers of 0.2×0.2 in the $\eta - \phi$ space. These trigger towers are further divided longitudinally into electromagnetic trigger towers and hadronic trigger towers.

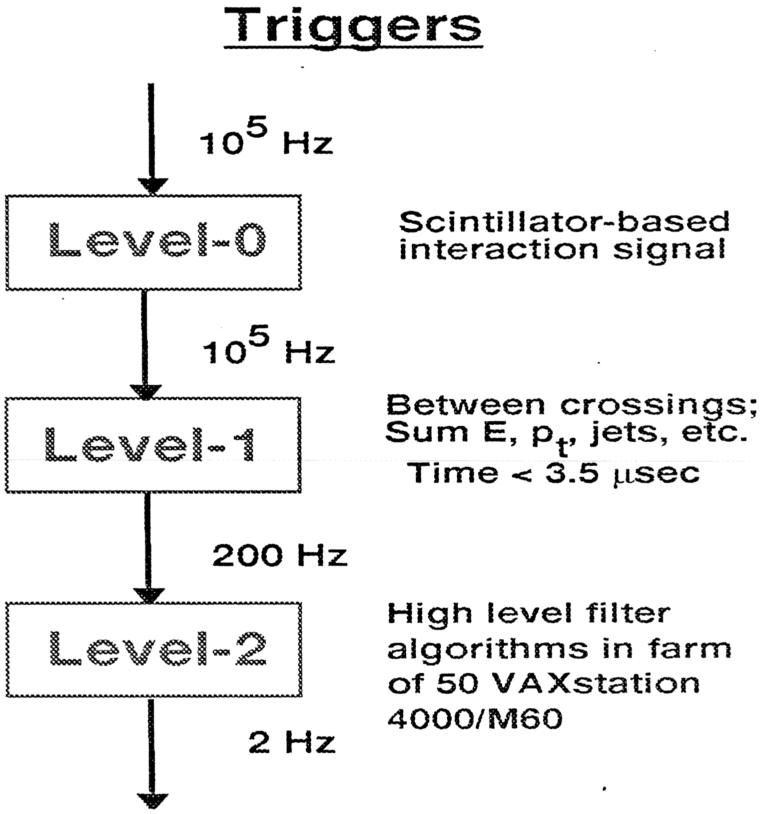

Figure 2.8: Three levels of trigger and their rates

Level 2 (Software triggers)

Once an event passes Level 1 it is shipped to the Level 2 system. Unlike the first two hardware triggers, Level 2 is a software trigger. The system is based on a farm of VAXstation 4000-60's which collect and process much of the raw data, perform a fast preliminary reconstruction, and decide whether or not the event should be kept. For this decision to be true the event must satisfy one of the 128 software filters. These filters are built out of a series of tools or algorithms. Typical algorithms are those which look for electromagnetic jets, hadronic jets, muons, missing transverse energy, etc. Figure 2.7 shows the trigger organization and trigger rates. (This chapter is written based on the following sources and their references : [32, 33, 34, 35])

Chapter 3

Data Analysis

3.1 Reconstruction

The event reconstruction is done with a D0 standard software package called D0RECO. This package converts the digitized raw data into the hit position, hit timing, and deposited energy in the detector which are then corrected with calibration data such as the amplifier gains, geometrical survey information, etc and then D0RECO reconstructs the kinematical parameters of particles.

3.1.1 Vertex

The central tracking information is used to reconstruct the vertex position. The following steps are taken to reconstruct the vertex.

- A fit is performed on the hits in the drift chambers to make a track in the rϕ plane.
- An rz track associated with the rϕ track is reconstructed.

- By projecting the reconstructed tracks onto the beam axis and performing a gaussian fit to the distribution of z intercepts, the z vertex position is obtained.

The vertex resolution is measured to be 0.65 cm to 0.95 cm in the z direction. If more than one vertex is identified in the event, the primary vertex is defined as the one with the maximum number of tracks.

3.1.2 Electron/Photon

The reconstruction of electrons or photons proceeds as follows: All EM towers are first ordered in decreasing transverse energy, E_T. An EM tower is defined as the four layers of the EM calorimeter plus the first layer of the fine hadronic calorimeter. One loops over all the towers above a threshold of $E_T > 50$ MeV, finds a nearest-neighbor tower which has the highest transverse energy. These neighboring towers are then linked together. If no nearest-neighbor exists a cluster is defined by a single tower, when it is an ensemble of towers which have been linked locally. Clusters with a total E_T of less than 1.5 GeV are not included. DØRECO requires that the fraction of energy outside the central tower must be less than 60% . The cluster centroid is calculated from a Log(E) weighted mean of the cell positions of EM layer three (recall that layer three is the most finely segmented in $\Delta\eta \times \Delta\phi$). For electrons, DØRECO requires that there be at least one track match in the CD (Central Detector) within $\Delta\eta \times \Delta\phi = 0.1 \times 0.1$.

The electron energy resolution is expressed as follows:

$$(\frac{\sigma}{E})^2 = C^2 + \frac{S^2}{E} + \frac{N^2}{E^2}$$

where E is the mean energy of the incident electron, C is a constant term which reflects calibration errors such as the momentum variation of the test beam and the thickness variation of the LAr gaps, S is the sampling fluctuation term due to the fluctuation of showers in the LAr gaps and N is the noise term including both electronic noise and noise induced by the radioactivity of the absorber. The measured values for the CCEM are

- $C = 0.003 \pm 0.002$
- $S = (0.140 \pm 0.005)\ \sqrt{\text{GeV}}$
- $N = 0.140\quad \text{GeV}$

The relative energy resolution of the ECEM as a function of energy was measured at the DØ test beam. The parameters in the resolution function are

- $C = 0.003 \pm 0.003$
- $S = (0.157 \pm 0.006)\ \sqrt{\text{GeV}}$
- $N = (0.290 \pm 0.030)\quad \text{GeV}$

The spatial resolution was also determined using 50 GeV electrons by comparing the beam track and the energy weighted position of the shower solely in the layer three of the ECEM. This resolution can be parameterized as

$$\sigma(\text{mm}) = 1.0 + 0.035 \times x^2$$

where x is the distance of the impact position in layer three from the edge of a tower.

3.1.3 Muon

The muon reconstruction in DØRECO is in three stages. The three stages are hit reconstruction, track finding and global track fitting. The hit reconstruction first finds potential muon hits based on the wire and pad signal information from the muon system. After correcting the data based on the survey information and chamber geometry, the hits are ordered and associated to 3-D space points. Pattern recognition code then attempts to group the hits into tracks loosely consistent with muons from the interaction region. Then the global fit is performed using the muon chamber track segments, energy deposit in the calorimeter, a track in the central detector and the vertex.

The momentum resolution is parameterized as [36]

$$\sigma(1/p)/(1/p) = \sqrt{(0.18(p-2)/p)^2 + ((0.003 \pm 0.001)p)^2}$$

where p is in GeV/c. Multiple coulomb scattering in the iron limits the relative momentum resolution to $\geq 18\%$ up to the limit imposed by the bend coordinate resolution of the proportional drift tubes.

3.1.4 Jet

A jet is defined as a collimated beam of particles resulting from the fragmentation of a parton. The energy and direction of a jet is measured with a fixed cone algorithm at DØ[37]. An energy vector $\vec{E} = (E_x, E_y, E_z)$ is assigned to each calorimeter tower. The transverse components of $\vec{E}$ are corrected using the z coordinate of the measured event vertex. The algorthim starts by finding a seed tower with 1 GeV, and proceeds by adding energies from the neighboring towers. The towers are added to the cluster up to a radius of 0.7 in $\eta - \phi$ space. If the final jet cone overlaps with any previously found jet cones, a decision is made whether to split two jets or merge the two into one jet. If the jets share more than 50% of their energies, they are merged, otherwise split. The jet threshold is chosen to be 10 GeV.

The jet E_T resolution can be parameterized as a function of E_T^{jet};

$$(\frac{\sigma}{E_T^{jet}})^2 = C^2 + \frac{S^2}{E_T^{jet}} + \frac{N^2}{E_T^{jet}} \tag{3.1}$$

where C is the error term from the calibration, the second term is due to the shower fluctuations in the sampling gap, and the third term is due to the detector noise and underlying event contribution. The fit values of these parameters have been obtained from data.

$$\begin{aligned} C &= 0.01 \pm 0.005 \\ S &= 0.74 \pm 0.07 \ \sqrt{\mathrm{GeV}} \\ N &= 2.16 \pm 0.22 \ \mathrm{GeV} \end{aligned} \tag{3.2}$$

A special technique was used for the jet energy scale correction. The D0 absolute jet energy correction is derived using events with just one photon and a jet. The missing E_T projection fraction (MPF) is defined by the following equation:

$$MPF = \frac{\vec{\not{E}}_T \cdot \hat{n}_{jet}}{E_T^{jet}} \tag{3.3}$$

where $\vec{\not{E}}_T$ is the missing energy vector, $\hat{n}_{jet}$ is the unit vector of the jet axis on the plane transverse to the beam axis. The relative response of the calorimeter to a jet is then

$$\frac{E_T^{jet}}{E_T^{\gamma}} = \frac{1}{1 + MPF} \tag{3.4}$$

The above relationship holds if there is one jet and one photon in the event which balance each other. [35] The procedure for computing the D0 jet energy scale correction is as follows:

- Select events with only one jet and one photon.

- Require the photon and the jet to be back to back in azimuth within 50 degrees.
- Determine a jet energy scale correction using relative response. The correction factor is the inverse of the relative response.
- Subtract energy contribution from the underlying events. The underlying events contribution is determined using data and is approximately 4 GeV.
- Scale up the jet energy to compensate the low absolute EM energy response at DØ. This scaling up is based on the Z mass comparison between DØ and the LEP experiments.

The typical size of the correction is $(16 \pm 5)\%$ at $E_T = 25$ GeV and $(24 \pm 5)\%$ at $E_T = 100$ GeV.

3.1.5 Missing Transverse Energy

The energy of neutrinos in an event is measured as the missing energy. The missing transverse energy is defined as the negative of the energy vector sum of all the final states in the transverse plane. Since the z component of the energy can not be accurately measured due to inadequate coverage in the forward direction, only the transverse components of the missing energy ($\not\!\!E_T$) is used. $\not\!\!E_T$ is corrected for the energy in the ICD and massless gaps. The calorimeter $\not\!\!E_T$, ($\not\!\!E_T^{cal}$), is defined as the $\not\!\!E_T$ measured using the calorimeter alone:

$$\begin{aligned}
\vec{\not\!\!E_T} &= -\sum_{j=1}^{n} \vec{E}_j \\
\not\!\!E_T^{cal} &= \sqrt{\not\!\!E_X^2 + \not\!\!E_Y^2}
\end{aligned}$$

where j runs over all cells in the calorimeter and E_j is the deposited energy in cell j. In the case of an event with muons, $\not{E}_T$ is calculated by including the measured muon momentum and subtracting the expected muon energy deposition in the calorimeter.

The $\not{E}_T$ resolution has been parametrized using a QCD dijet data sample which most often contains no real $\not{E}_T$. The $\not{E}_T$ resolution of the detector is as follows:

$$\sigma = a + b \times S_T + c \times S_T^2$$

where S_T is the summed transverse energy in the calorimeter and

$a = (1.89 \pm 0.05)$ GeV

$b = (6.7 \pm 0.7) \times 10^{-3}$ GeV

$c = (9.9 \pm 2.1) \times 10^{-6}$ GeV^{-1} [38] .

3.2 Particle Identification (ID)

3.2.1 Electron ID

As described before, electrons are identified as an electromagnetic shower in the calorimeter with an associated track in the central tracking system. Further requirements are imposed for the electrons as follows:

- EM fraction

  $\frac{EM\ ENERGY}{TOTAL\ ENERGY} > 0.90$

  This requirement uses the longitudinal shower shape to differentiate an EM shower from a hadronic one. It is required that at least 90% of the cluster energy must be contained within the EM calorimeter. Hadrons, on the average, deposit less than 10% of their energy in the electromagnetic section of the calorimeter.

Therefore, this cut provides powerful discrimination against hadrons and is more than 99% efficient for energies between 10 and 150 GeV.

- Isolation

  $\frac{E_{TOT}(CONE\ 0.4)-E_{EM}(CONE\ 0.2)}{E_{EM}(CONE\ 0.2)} < 0.10$

  where E_{TOT}(CONE 0.4) is the total energy deposited in a cone $\Delta R = 0.4$ ($\Delta R = \sqrt{\Delta\eta^2 + \Delta\phi^2}$) and E_{EM}(CONE 0.2) is the total energy deposited in the EM layers in a cone $\Delta R = 0.2$. This cone is drawn from the event vertex to the center of gravity of the electromagnetic cluster. This requirement uses the transverse shower shape to differentiate an isolated EM shower from a hadronic shower.

- Track match significance

  $\sigma_{TRACK} \leq 10$

  The significance is defined as:

  $$\sigma_{TRACK} = \sqrt{(\frac{R\Delta\phi}{R\delta\phi})^2 + (\frac{\Delta z}{\delta z})^2}$$

  where R is the radial distance from vertex to the center of the candidate EM shower in cm, $\Delta\phi$ and Δz are the difference between the track position and the shower center in azimuthal angle (rad) and the beam direction (cm), respectively. $R\delta\phi$ and δz are the position resolution of the calorimeter in the azimuthal and beam directions, respectively. Track match significance between the reconstructed track and the calorimeter cluster is required to be less than 10. This cut removes photons and fakes from the data sample.

- dE/dx Requirement

  Due to the absence of a central magnetic field in the detector, the e^+e^- pairs from photon conversions overlap in space. The ionization per unit length dE/dx

in the drift chambers can be used to discriminate multiple tracks from a single track. $dE/dx \sim 1$ mip (minimum ionizing particle) indicates a single electron. $dE/dx \sim 2$ mip is an electron-positron pair from photon conversion. A Monte Carlo study shows that $dE/dx \sim 3$ mip belongs to an electron along with its radiative photon. A track with $1.6 < dE/dx(\text{mip}) < 3.0$ for CC and $1.6 < dE/dx(\text{mip}) < 2.6$ for EC is rejected.

- Covariance matrix χ^2_H

  χ^2_H (≤ 100 CC, ≤ 100 EC)

  The shower shape may be characterized by the fraction of the cluster energy deposited in each layer of the calorimeter. These fractions are also dependent on the incident electron energy. However, these fractions are correlated, *i.e.*, a shower which fluctuates and deposits a large fraction of its energy in the first layer will then deposit a smaller fraction in the subsequent layers and vice versa.

  To simultaneously take into account both the energy observed in a given layer and its correlations with the energy deposited in the other layers, a covariance matrix (M) of 41 observables x_i was developed to characterize the "electron-ness" of the shower. The matrix elements are computed from a parent sample of N Monte Carlo electrons with energies ranging between 10 GeV to 150 GeV. They are defined as :

$$M_{ij} = \frac{1}{N}\sum_{n=1}^{N}(x_i^n - \bar{x}_i)(x_j^n - \bar{x}_j) \tag{3.5}$$

  where x_i^n is the value of the i^{th} observable for the n^{th} electron and $\bar{x}_i$ is the mean of the i^{th} observable. The observables are the fraction of shower energy in the first layer (EM1), the second EM layer (EM2), the fourth EM layer (EM4) and the fraction of shower energy in each cell of a 6 × 6 array centered on the hottest tower in the third EM layer (EM3). To include the energy and impact parameter dependence into the matrix, the logarithm of the total energy and the position of the event vertex were added to the covariance matrix (M).

For a shower, characterized by the observable $\acute{x}_i$, the covariance parameter

$$\chi^2_H = \sum_{ij}^{41} (\acute{x}_i - \bar{x}_i) H_{ij} (\acute{x}_j - \bar{x}_j) \tag{3.6}$$

where $H = M^{-1}$, measures how consistent its shape is with the expected shape from an electromagnetic shower. The requirement of $\chi^2_H < 100$ is about 94% efficient for electrons with a rejection factor of around 4 against EM clusters that are not due to electrons.

The efficiencies for the above cuts were measured using $Z \rightarrow e^+e^-$ data and are listed in Table 3.1 [39].

3.2.2 Muon ID

The sources of background for an isolated muon track are cosmic ray muons, combinatorics, hadron punchthrough and decay muons from π, K, b and c particles in QCD jets. The following requirements were imposed on the candidate tracks to reduce these backgrounds.

- $|\eta| \leq 1.7$

  We use muons in the WAMUS(Wide Angle MUon System) detector only which corresponds to the η region of $|\eta| \leq 1.7$.

ϵ	CC	EC
$(EM\ Fraction, Isolation, \chi^2_H)$	0.902 ± 0.013	0.921 ± 0.033
Track in Road	0.879 ± 0.022	0.820 ± 0.024
σ_{TRACK}	0.975 ± 0.005	0.898 ± 0.017
dE/dx	0.944 ± 0.011	0.752 ± 0.037

Table 3.1: The electron selection efficiencies for CC and EC.

- $\int B \cdot dL \geq 0.6$ GeV

  In order to reject the muons that pass through the gap between the CF and the EF toroids and have a poor momentum determination, the total amount of magnetic field along the muon track is required to be $\int B \cdot dL \geq 0.6$ GeV. This roughly removes the tracks in the region of $0.8 < |\eta| < 1.0$ where the detector has only 9 interaction lengths, as compared to 13–18 interaction lengths elsewhere.

- IFW4 ≤ 1

  The muon reconstruction program calculates several quantities that provide information on the quality of the track during the track fitting stage. They are the quality of the track fit both in the bend and in the non-bend view, the impact parameters of the extrapolated muon track in both views, the number of hits associated with a given track, and the number of hits used to fit the track. The Muon Quality Flag (IFW4) is defined as the number of quantities that fail the standard cuts. Only tracks with IFW4$\leq$ 1 are accepted.

- Calorimeter Energy(Muon Cell + 1NN) ≥ 1.0 GeV for both CF and EF

  In order to reduce cosmic and combinatoric muons from the data sample it is required that the deposited energy in the calorimeter be consistent with the passage of a minimum ionizing particle.

- CD Track Match

  $\Delta\phi(\mu, CD) \leq 0.45$ and $\Delta\theta(\mu, CD) \leq 0.45$

  The muon candidate track is required to have a matching track in the central detector. This cut reduces the combinatoric muons.

- $|$3-D Impact Parameter$| < 22$ *cm*

  The 3-D impact parameter is calculated by extrapolating the muon trajectory outside the magnet back towards the vertex and is the distance of the closet approach to the reconstructed vertex. This cut reduces cosmic and combinatoric muons.

- Muon isolation

  Decay muons from π, K, b and c particles in the QCD jets can be effectively removed by invoking isolation criteria. The following two-fold requirements are used:

  - $I_\mu \leq 5\sigma$

    The isolation variable I_μ is measured by summing the calorimeter energy in cells hit by the muon and their two nearest neighbors, then subtracting the expected contribution from the muon ionization and dividing the difference by the expected error.

  - Halo cut $E(0.6) - E(0.2) \leq 8$ GeV

    The halo cut is defined as the difference in the energy deposited in a cone of 0.6 and 0.2 around the muon in the calorimeter.

- Floating time cut : $t_0^f \leq 100ns$

  The timing of muon track at the muon chambers with regard to the beam crossing is calculated by floating t_0 in the muon reconstruction program. This cut is used only in the $\mu^+\mu^-$ channel in order to remove cosmic muons.

3.3 Monte Carlo studies

The results from a complex experiment such as the one described in this thesis must be interpreted with the help of detailed computer simulations of the experiment. The simulation involves a large number of variables that represent the experiment and is usually carried out with a Monte Carlo method. Monte Carlo simulation is also used to optimize the design of experiments. In particle physics experiments, Monte Carlo simulation consists of three steps. The first step is to simulate physics processes using theoretical calculations and models based on the experimental measurements. This step is called event generation. The second step is to simulate the responses from the detector of the experiment and is called the detector simulation. At the end of the second step, Monte Carlo data has the identical format of the experimental data. The third step is to process the Monte Carlo generated data in the same way as the experimental data.

Three alternate Monte Carlo simulation methods are used in this analysis, depending on the purpose of study and the characteristic of the program. ISAJET and PYTHIA event generators, DØGEANT detector simulation package and DØRECO reconstruction program are used when a realistic modelling is essential, such as, for example the estimation of detection efficiency for $W^+W^- \rightarrow l^+l^-$ process the standard model couplings. This method is called the Full Simulation. The background from $Z \rightarrow e^+e^-$ and $\mu^+\mu^-$ are estimated using the ZKIN fast simulation program which is based on the parameterization of detector response. Since neither ISAJET nor PYTHIA can generate non-Standard Model W pair events, a program written by D. Zeppenfeld and U. Baur is used to estimate the detection efficiencies of such events.

3.3.1 Full Simulation

DØGEANT

DØGEANT is the DØ implementation of the CERN detector simulation program GEANT [41]. The geometry and materials of the DØ detector are input parameters to GEANT. GEANT simulates interactions between particles and tracks particle through the defined geometry of the detector. These processes are ionization energy loss, δ-ray production, electromagnetic shower generation (which includes multiple coulomb scattering, compton scattering, pair creation and bremsstrahlung), hadronic shower generation (which includes elastic and inelastic nuclear interactions, neutron capture and nuclear fission) and particle decays. Each particle is tracked down to the preset minimum energies that depend on the process. In D0GEANT, the minimum energies are set to 10 keV for all processes. The step size of the track depends on the medium and is chosen so that the simulated distributions reproduce the measured ones.

MU-SMEAR Monte Carlo

In order to take into account the actual position resolutions and inefficiencies of the muon chamber system, an intermediate program, MU-SMEAR was written [42]. The MU-SMEAR program takes the output from D0GEANT and applies smearing, based on measured values, to the muon chamber hits. The differences between ideal resolutions and efficiencies in D0GEANT and measured values are due to gas leaks, the alignment of the muon chamber system and so on. There are three steps in MU-SMEAR. D0GEANT generates hits using a position resolution of 200 microns in drift direction and a position resolution of 12 cm with pad measurement. MU-SMEAR smears them to reproduce 700 microns and 20 cm which are the measured values. Secondly, MU-SMEAR eliminates hits due to the chamber inefficiencies for each module. Third, the geometry parameters are adjusted in order to reproduce the observed momentum resolution. A very good agreement between Z data and Monte Carlo has been obtained by using MU-SMEAR [42].

ISAJET/PYTHIA Monte Carlo

The ISAJET and PYTHIA Monte Carlo programs are used as event generators for background and efficiency calculations whenever possible. They simulate $p\bar{p}$ interactions at high energy [43, 44]. These Monte Carlos are based on perturbative QCD calculation and phenomenological models for parton fragmentation. Events are generated in four steps:

- Hard Scattering

  A primary hard-scattering is generated according to the appropriate QCD cross-section.

- QCD Evolution

  QCD radiative corrections are taken into account for both initial- and final-state radiations.

- Hadronization

  Partons are fragmented into hadrons.

- Beam Fragmentation

  The leftover beam partons also undergo the hadronization process which basically creates minimum bias events.

The main difference between ISAJET and PYTHIA is at the hadronization process. ISAJET uses the Feynman-Field fragmentation scheme and approximates scaling of the energy fraction distributions observed in quark jets [45]. On the other hand, PYTHIA uses the standard Lund string fragmentation [46].

3.3.2 ZKIN Monte Carlo

The major background for $W^+W^- \rightarrow e^+e^-(\mu^+\mu^-)$ channel is the $Z \rightarrow e^+e^-(\mu^+\mu^-)$ events. Its cross section times branching ratio is 3 orders of magnitude higher than

$W^+W^- \rightarrow e^+e^-(\mu^+\mu^-)$ events. We need at least 4 orders of magnitude reduction in the background and therefore need more than 10^5 $Z \rightarrow e^+e^-(\mu^+\mu^-)$ Monte Carlo events in order to reliably estimate the background from this source. It is practically impossible to generate 10^5 events with the standard ISAJET/PYTHIA + D0GEANT. Instead, a fast simulation program (ZKIN) for $Z \rightarrow e^+e^-$ developed at the D0 collaboration in conjunction with the W and Z cross section measurements is used. This program has been modified to generate $Z \rightarrow \mu^+\mu^-$ events as well.

The ZKIN Monte Carlo program is based on a double differential cross section, $d^2\sigma/(dp_T^Z \times dy^Z)$, calculated by Arnold and Kauffman [47] at the next to leading order where p_T^Z and y^Z are the transverse momentum and rapidity of the Z, respectively. The Z is produced at p_T^Z and y^Z according to Arnold and Kauffman distribution and then decays into e^+e^-. Proper angular distributions and decay kinematics for the final states are taken into account. The $\not{E}_T$ due to the underlying events, mismeasured electrons, and the detector resolution are incorporated by using the measured missing E_T distribution from the data [48]. Figure 3.4 and Figure 3.5 shows a comparison between PYTHIA-D0GEANT and ZKIN Monte Carlo events for $Z \rightarrow e^+e^-$ and $\mu^+\mu^-$, respectively.

3.3.3 ZEPPENFELD-BAUR & D0-FAST Monte Carlo

Since neither ISAJET nor PYTHIA is able to generate W pair production events with the non-Standard Model couplings, a program developed by D. Zeppenfeld and U. Baur [49] is used to generate the W pair production events with the non-Standard Model couplings. The detection efficiencies for W pair events with the non-Standard Model couplings are calculated using this program with a simplified and fast detector simulation program (DØ-FAST). The compatibility of this procedure with the standard ISAJET/PYTHIA + DØGEANT method is tested by comparing the distributions of kinematical variables of generated events with the Standard Model couplings. The DØ-FAST program reads the output in the form of kinematical variables of generated particles from the Zeppenfeld-Baur program which also supplies the cross section weight corrected for the K-factor [21, 49]. The PDFLIB supplies different structure functions for the DØ-FAST program.

The DØ-FAST detector simulation is explained briefly in the following:

- Energy resolution of electron

  The energy of the electron is smeared using the parameterized energy resolution [32],

  $$\sigma_E = \sqrt{S^2/E + (0.003)^2} \times E \tag{3.7}$$

  where $S = 0.14$ for $|\eta_e| < 1.1$ and $S = 0.157$ for $|\eta_e| \geq 1.1$ and $|\eta_e| < 4.0$.

- Momentum resolution of muon

  The momentum of muon is smeared using the parameterized momentum resolution [50],

  $$\sigma_p = \sqrt{(0.18)^2 + (0.006 \times p)^2} \times p. \tag{3.8}$$

- Missing E_T

  The missing E_T is calculated from the momenta of neutrinos in the Zeppenfeld-Baur program and smeared using the measured missing E_T distribution from the data. The effects on $\not{E}_T$ due to the underlying events and the detector resolution are incorporated by this smearing [48].

- Fiducial cuts

  The electrons in the CC - EC transition region ($1.1 \leq |\eta_e| \leq 1.5$) are discarded, since their energies are poorly measured.

- Efficiencies

  The electron and muon detection efficiencies measured from data or estimated from Monte Carlo studies are included in the D0-FAST detector simulation. The measured trigger efficiencies are also included.

Event Generator	PDF *	No of Events	Acceptance
D0-FAST	MRSD-	25000	0.220 ± 0.003
PYTHIA-D0GEANT	EHLQ	2485	0.208 ± 0.010
ISAJET-D0GEANT	MRSD-	1500	0.229 ± 0.014

Table 3.2: The acceptance for $W^+W^- \rightarrow e^+e^-$ with different event generators.

(* Parton Distribution Functions)

Figure 3.1 shows the distributions of M_{ee}, $\not\!\!E_T$, E_T^{e1}, and E_T^{e2} for the W pair Monte Carlo events with the SM couplings (generated with PYTHIA and D0GEANT). The distributions from D0-FAST are also shown for comparison. Table 3.2 shows the acceptance for SM W pair production using different event generators. Figure 3.2 shows the distributions of E_T^e, p_T^μ and $\not\!\!E_T$ for the W pair Monte Carlo events with the SM couplings (generated with PYTHIA and D0GEANT). The distributions from

DØ-FAST are also shown for comparison. Figure 3.3 shows the distributions of $p_T^{\mu 1}$, $p_T^{\mu 2}$ and E_T^{η}. E_T^{η} is defined as the projection of $\vec{\not{E}_T}$ onto the bi-sector of the decay angles of two muons.

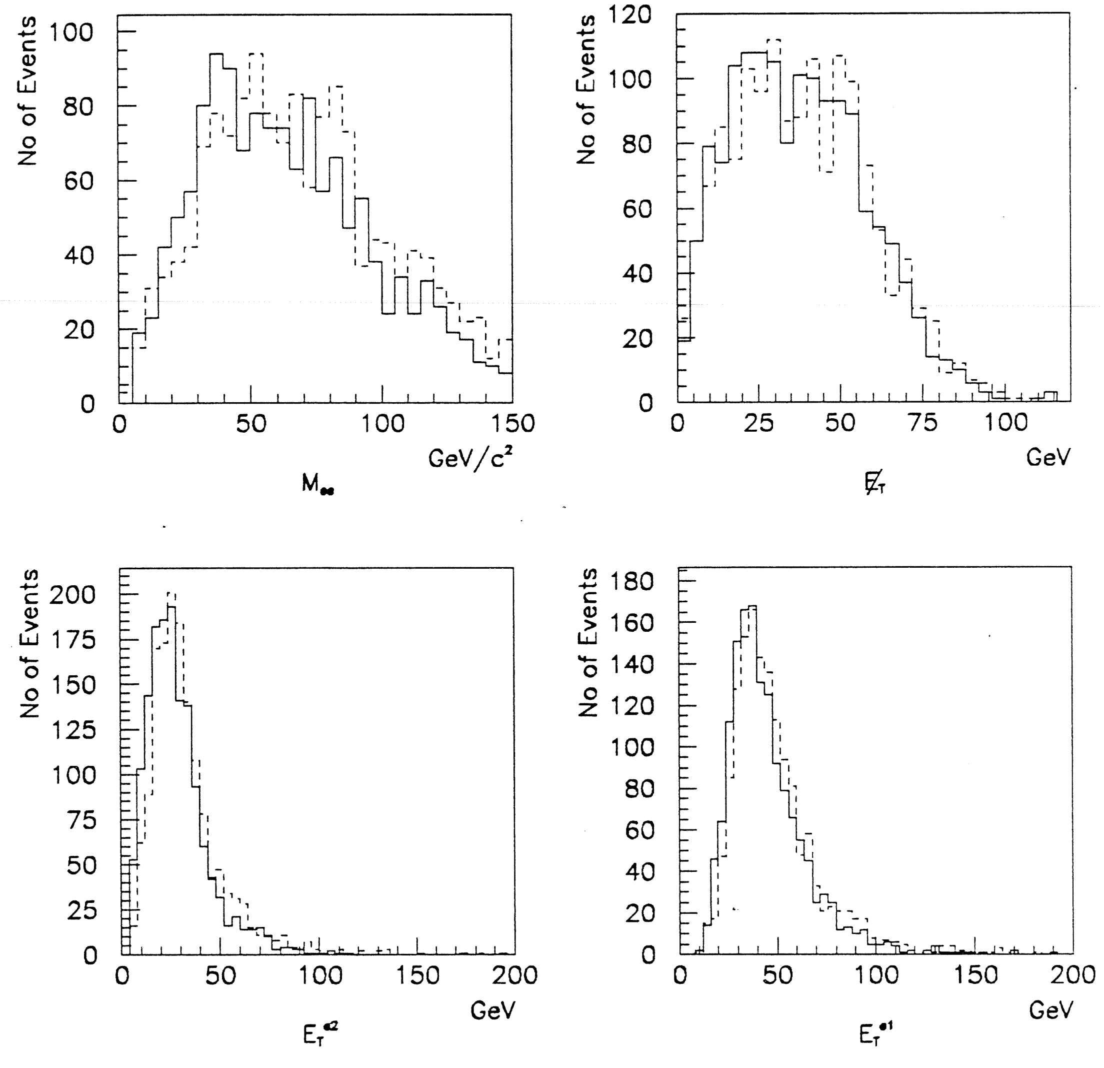

Figure 3.1: The distributions of the invariant mass of e^+e^- system, $\not{E}_T$, E_T^{e1} and E_T^{e2} for the W pair Monte Carlo events. The solid and dashed lines indicate PYTHIA-DØGEANT and DØ-FAST, respectively.

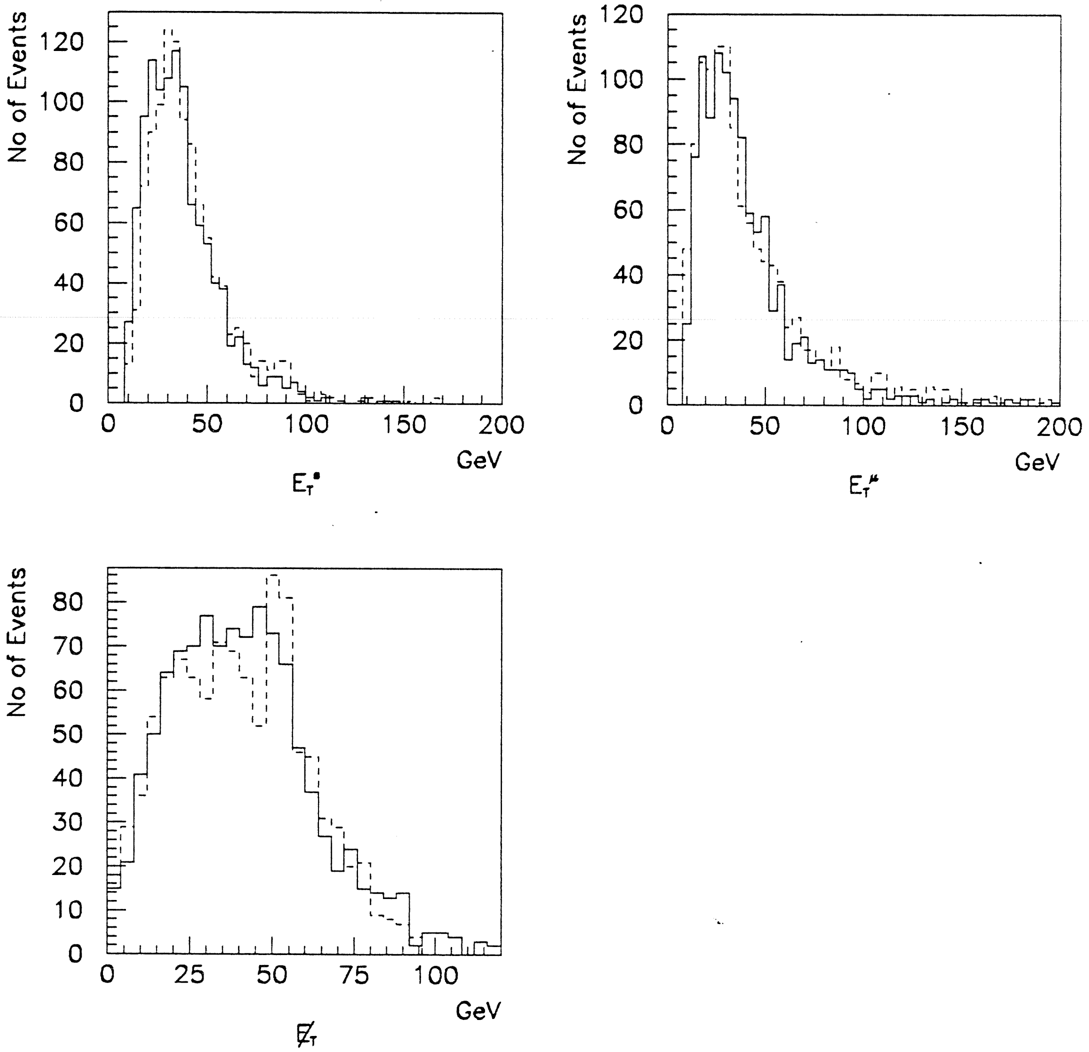

Figure 3.2: The distributions of E_T^e, p_T^μ, and $\not\!\!E_T$ for the $W^+W^- \to e^\pm\mu^\mp$ Monte Carlo events. The solid and dashed lines indicate PYTHIA-D0GEANT and D0-FAST, respectively.

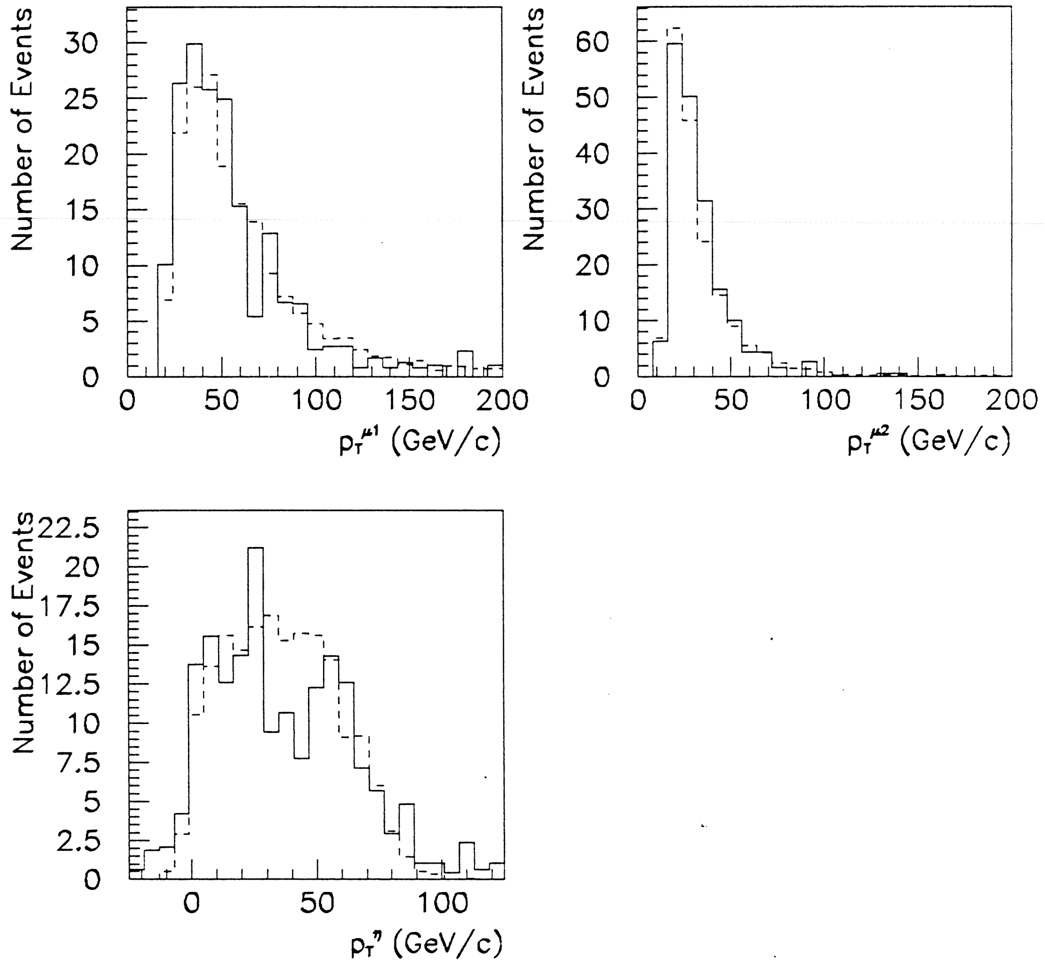

Figure 3.3: The distributions of $p_T^{\mu 1}$, $p_T^{\mu 2}$, and p_T^{η} for the $W^+W^- \rightarrow \mu^+\mu^-$ Monte Carlo events. The solid and dashed lines indicate PYTHIA-D0GEANT and D0-FAST simulations, respectively.

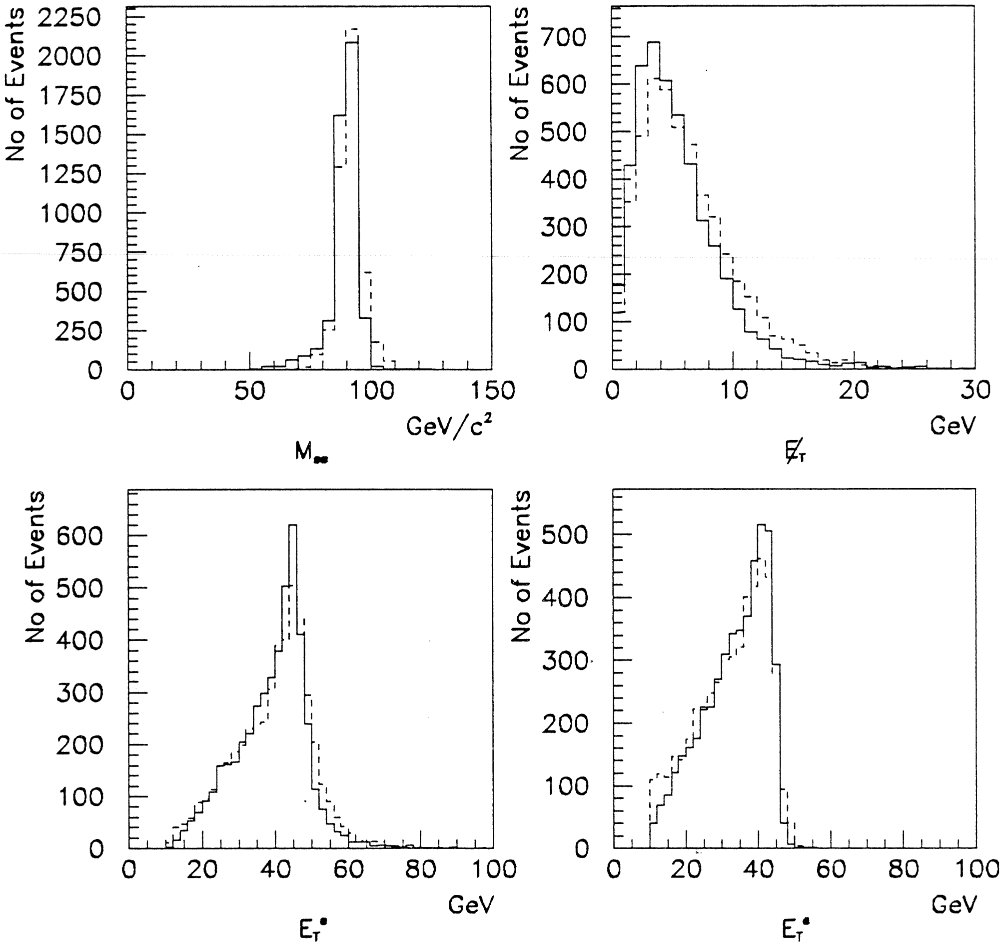

Figure 3.4: The distributions of the invariant mass, $\not\!\!E_T$, E_T^{e1} and E_T^{e2} for $Z \rightarrow e^+e^-$ events. The solid lines and dashed lines indicate PYTHIA-D0GEANT and ZKIN Monte Carlo events, respectively.

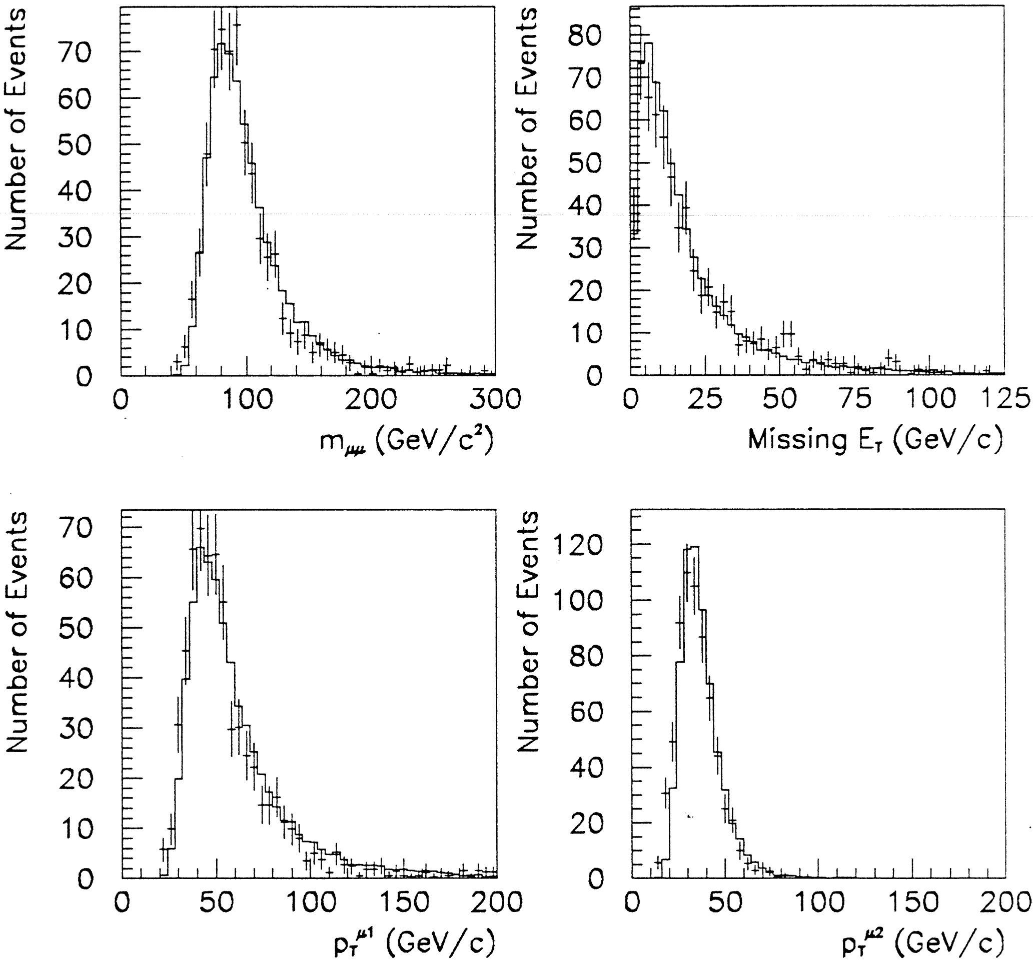

Figure 3.5: The distributions of the invariant mass, $\not{E}_T$, $p_T^{\mu 1}$ and $p_T^{\mu 2}$ for $Z \rightarrow \mu^+\mu^-$ events. The solid lines indicate the ZKIN Monte Carlo and the data points with error bars indicate the PYTHIA-D0GEANT events.

3.4 Search for $W^+W^- \rightarrow e^+ + e^- + X$

3.4.1 Luminosity, Trigger and Data Sample

A full data set from the collider run Ia (1992-1993) is used in the e^+e^- mode analysis. The luminosity for this data set is estimated to be $\int \mathcal{L}dt = 13.9 \pm 1.7pb^{-1}$. The trigger for this mode is ELE-2-HIGH which required two EM clusters with E_T greater than 7 GeV at level 1 and two isolated EM towers with E_T greater than 10 GeV at level 2.

3.4.2 Event Selection

The following cuts were applied to an event with two isolated electrons:

- $E_T^{e1} \geq 20$ GeV and $E_T^{e2} \geq 20$ GeV

  where e1 and e2 indicate the electrons with higher and lower E_T, respectively.

- $\not{E}_T \geq 20$ GeV

- $M_{ee} \leq 77$ GeV/c^2 or $M_{ee} \geq 105$

  where M_{ee} is the invariant mass of dielectron system. This cut is used to reject $Z \rightarrow e^+e^-$ events.

- For $\Delta\phi(E_T^{e2},\not{E}_T) < 20^o$ or $\Delta\phi(E_T^{e2},\not{E}_T) > 160^o$, $\not{E}_T \geq 50$ GeV

  where $\Delta\phi(E_T^{e2},\not{E}_T)$ is the angle between the lower E_T electron and the missing energy. This cut is imposed to eliminate $Z \rightarrow \tau^+\tau^- \rightarrow e^+e^-$ events and $Z \rightarrow e^+e^-$ events with mis-measured electron energies. The restriction on the $\not{E}_T$ is applied to keep the detection efficiencies for W pair production with the non-Standard Model couplings high. Figure 3.6 shows the 2-dimensional distributions of $\Delta\phi(E_T^{e2}, \not{E}_T)$ vs $\not{E}_T$ for W pair production events with the SM couplings (generated with PYTHIA-D0GEANT), $Z \rightarrow e^+e^-$ events (generated with PYTHIA-D0GEANT), and $Z \rightarrow \tau^+\tau^- \rightarrow e^+e^-$ events (generated with PYTHIA-D0GEANT), and W pair events with the non-SM couplings; $\Delta\kappa = 2$ and $\lambda = 0$ (generated with Zeppenfeld - D0-FAST).

- $|\vec{E_T}^{had}| \leq 40\text{GeV}$

  The $\vec{E_T}^{had}$ is defined as

  $$\vec{E_T}^{had} = -(\vec{E_T}^{e1} + \vec{E_T}^{e2} + \vec{\not{E}_T})$$

  This cut is designed to reduce the background from $t\bar{t}$ production which is expected to have jet activity associated with it. Figure 3.7 shows the distributions of the $|\vec{E_T}^{had}|$ for the W pair events with the SM couplings (PYTHIA-D0GEANT) and $t\bar{t}$ events with $m_{top} = 170$ GeV/c^2 (PYTHIA-D0GEANT). See [51] for the discussion on the systematic errors of this cut.

After these cuts, one event survives. Table 3.3 shows the breakdown of the numbers of events after each cut. The characteristics of the surviving event is shown in Table 3.4. The LEGO plot of the candidate event is shown in Figure 3.8.

Event Selection Cut	Number of Events
Trigger+ID	771
$E_T \geq$ 20 GeV	605
$\not{E}_T \geq$ 20 GeV	5
$M_{ee} \leq 77\text{GeV/c}^2$ or $M_{ee} \geq 105$	3
$\Delta\phi(E_T^{e2},\not{E}_T)$ cut	1
$\lvert\vec{E_T}^{had}\rvert \leq 40\text{GeV}$	1

Table 3.3: The numbers of events after event selection cuts for e^+e^- channel.

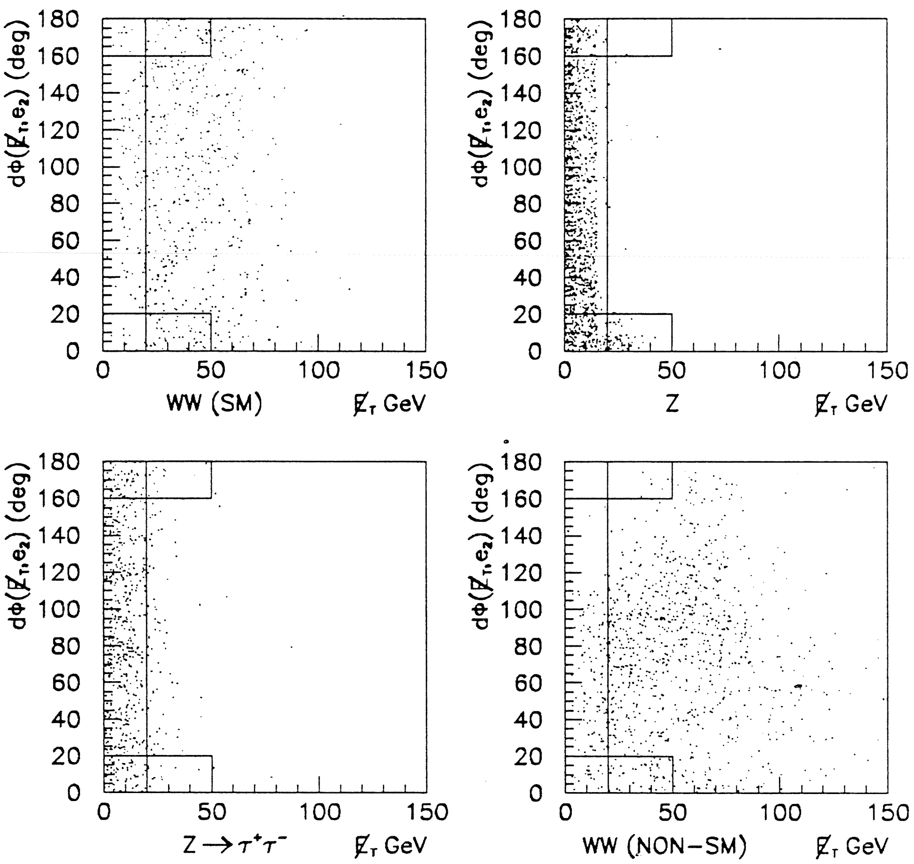

Figure 3.6: The 2-dimensional distributions of $\Delta\phi(E_T^{e2}, \not\!\!E_T)$ vs $\not\!\!E_T$ for W pair production events with the SM couplings (PYTHIA-D0GEANT), $Z \rightarrow e^+e^-$ events (PYTHIA-D0GEANT), $Z \rightarrow \tau^+\tau^- \rightarrow e^+e^-$ (PYTHIA-D0GEANT) events, and W pair events with the non-SM couplings (Zeppenfeld-D0FAST).

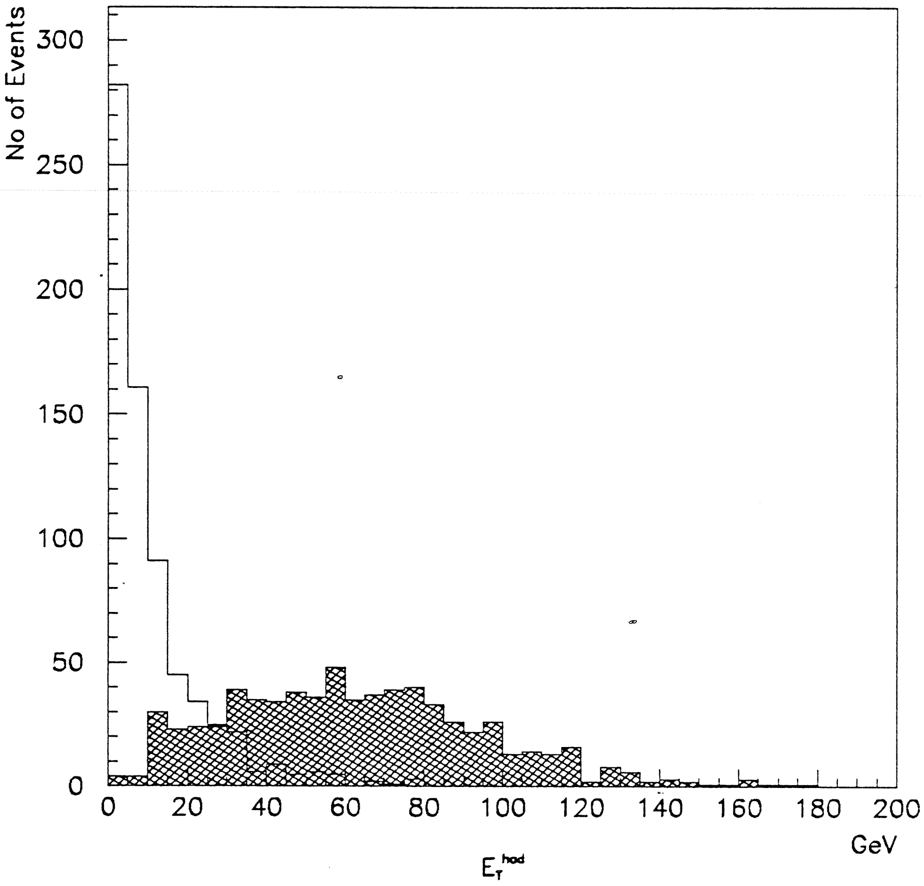

Figure 3.7: The distributions of the $|\vec{E_T}^{had}|$ for the $W^+W^- \rightarrow e^+e^-$ events with the SM couplings and $t\bar{t}$ events with m_{top} = 170 GeV/c^2 (hatched histogram).

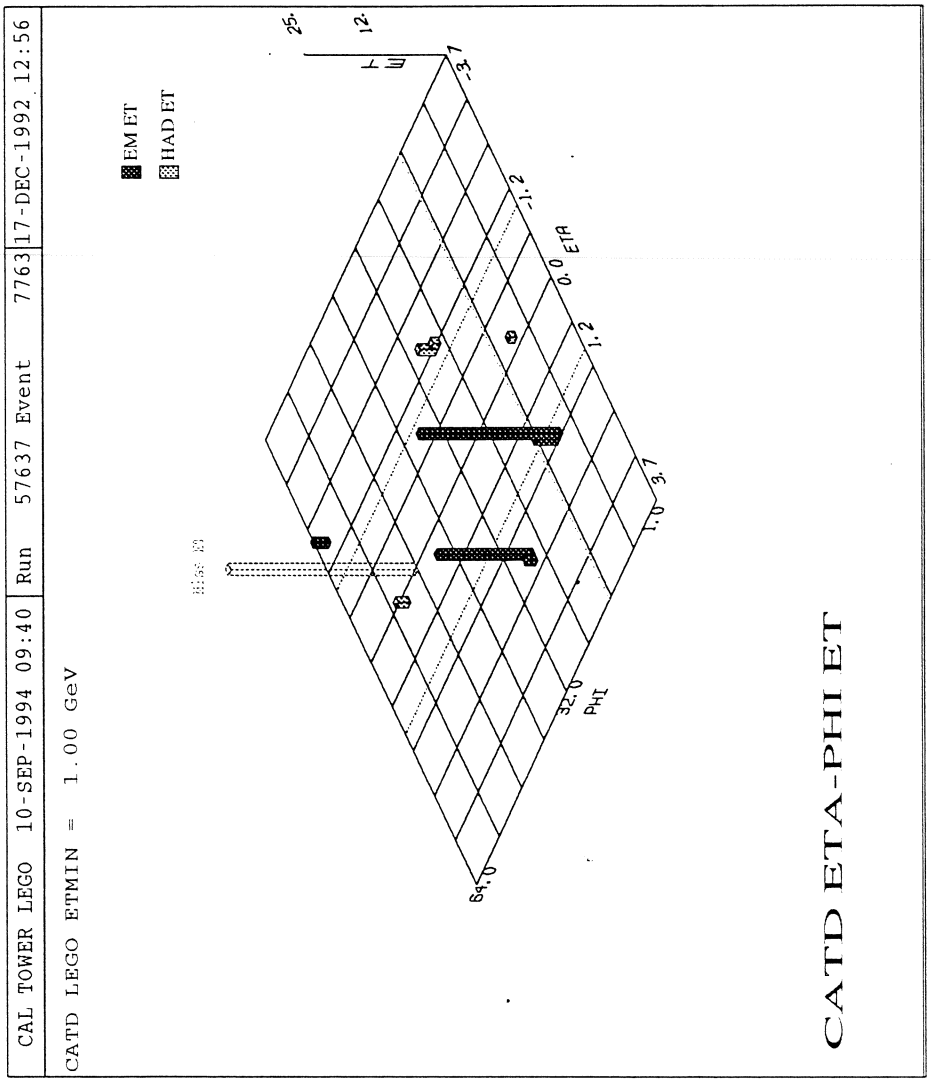

Figure 3.8: The candidate event for $W^+W^- \rightarrow e^+e^-$.

Run 57637		Event 7763			
	Electron 1	Electron 2	$\not{E}_T$	Jet 1	Jet 2
E_T	32GeV	23GeV	35GeV	15GeV	15GeV
η	1.6	2.1			
EM fraction	0.99	0.99			
Isolation	0.015	0.015			
χ^2_H	19.2	26.5			
Track match	0.6	0.6			
dE/dx	0.84	1.12			
$M_{ee} = 39\text{GeV/c}^2$			$M_T(ee, \not{E}_T) = 90\text{GeV/c}^2$		
$\Delta\phi(e_1, \not{E}_T) = 157^o$			$\Delta\phi(e_2, \not{E}_T) = 122^o$		
$\Delta\phi(e_1, e_2) = 82^o$			$E_T^{had} = 8\text{GeV}$		

Table 3.4: Characteristics of the surviving e^+e^- event.

3.4.3 Efficiency

The trigger efficiency has been calculated with the TRIGSIM simulation package as $\epsilon_{trig} = 0.989 \pm 0.002$. Table 3.5 shows the electron selection efficiencies in the different fiducial regions. The detection efficiency of $W^+W^- \rightarrow e^+e^-$ is estimated from a combination of Monte Carlo and data studies. The same particle selection requirements and event selection cuts as data are applied to the W pair Monte Carlo events (PYTHIA-D0GEANT). The number of events that survive all the cuts in each fiducial region is recorded as $N_{CC,CC}$, $N_{CC,EC}$ and $N_{EC,EC}$. The detection efficiency is calculated as

$$\begin{aligned} \epsilon_{ee} &= \frac{1}{N^{MC}_{Gen}} \left(N_{CC,CC}\ \epsilon^{CC,CC}_{ID+TRIG} + N_{CC,EC}\ \epsilon^{CC,EC}_{ID+TRIG}\right. \\ &+ \left. N_{EC,EC}\ \epsilon^{EC,EC}_{ID+TRIG}\right) \end{aligned} \tag{3.9}$$

where N^{MC}_{Gen} is the total number of generated events, and $\epsilon_{ID+TRIG}$ are the combined trigger and electron selection efficiencies.

Fiducial region	ϵ_{ID}	Acceptance
CC - CC	0.532 ± 0.041	0.125 ± 0.008
CC - EC	0.372 ± 0.044	0.064 ± 0.005
EC - EC	0.260 ± 0.058	0.019 ± 0.003

Table 3.5: The selection efficiencies for $W^+W^- \rightarrow e^+e^-$ events.

From 2485 Monte Carlo $W^+W^- \rightarrow e^+e^-$ events, the following events survive all the cuts: $N_{CC,CC} = 311$, $N_{CC,EC} = 159$, and $N_{EC,EC} = 48$. The overall detection efficiency is estimated to be

$$\epsilon_{ee} = 0.094 \pm 0.008. \tag{3.10}$$

The uncertainty on the overall efficiency includes uncertainties due to electron identification, acceptance and trigger. The number of expected signal events is calculated to be

$$N^{SM}_{expected}(W^+W^- \to e^+e^-) = 0.152 \pm 0.013(\text{stat}) \pm 0.024(\text{syst}). \tag{3.11}$$

The systematic error consists of a 10% error on the W pair cross section error due to the choice of the structure function; $\sigma \cdot Br(W^+W^- \to e^+e^-) = 0.12 \pm 0.01$ pb, and a 12% luminosity error.

3.4.4 Background

There are two types of background that compete with $W^+W^- \to e^+e^-$ process. One is the background event which has a similar event structure to the $W^+W^- \to e^+e^-$ process, such as $Z \to e^+e^-$, $Z \to \tau^+\tau^- \to e^+e^-$, $W^\pm\gamma \to e^\pm\gamma$ (γ is mis-identified as an electron), Drell-Yan production of e^+e^- pair, and $t\bar{t} \to e^+e^-$ processes. Such events are called *Physics* background. The other is the background event in which one or more electrons are mis-identified hadronic jets. Such events are called *Fake* background. Estimation of these background estimation are discussed in the following:

- Physics Background

1. $Z \rightarrow e^+e^-$

   A fast Z Monte Carlo (ZKIN) is used to estimate this background. From 150000 events generated by ZKIN Monte Carlo, 2 events survive all the cuts. The background from this source is estimated to be

   $$N_{background}(Z \rightarrow e^+e^-) = 0.020 \pm 0.014(\text{stat}) \pm 0.003(\text{syst}). \quad (3.12)$$

   Systematic error consists of 12% error on the luminosity and error from the Z cross section, $\sigma \cdot Br(Z \rightarrow e^+e^-) = 0.21 \pm 0.03$ nb.

2. $Z \rightarrow \tau^+\tau^- \rightarrow e^+e^-$

   $Z \rightarrow \tau^+\tau^- \rightarrow e^+e^-$ events are generated using PYTHIA-DØGEANT and reconstructed with DØRECO11.19. From 2000 generated events none of them survive. The background events from this source is estimated to be

   $$N_{background}(Z \rightarrow \tau^+\tau^-) < 10^{-3}. \quad (3.13)$$

3. $W^\pm\gamma \rightarrow e^\pm\gamma(\gamma \rightarrow e^\mp)$

   2500 $W\gamma$ events are generated with PYTHIA-DØGEANT and reconstructed with DØRECO11.19. The expected number of events from this source is

   $$N_{background}(W^\pm\gamma \rightarrow e^\pm\gamma) = 0.022 \pm 0.004(\text{stat}) \pm 0.022(\text{syst}). \quad (3.14)$$

   A 12% error on the luminosity and a 10% error in the cross section are taken into account in the systematic error.

4. $Drell - Yan \rightarrow e^+e^-$

   Drell-Yan events are generated in five invariant mass ranges (2000 events for each mass region): $80 < m_{DY} < 100$ GeV/c^2, $100 < m_{DY} < 150$ GeV/c^2,

$150 < m_{DY} < 200$ GeV/c^2, $200 < m_{DY} < 250$ GeV/c^2, and $250 < m_{DY} < 300$ GeV/c^2. The total number of background events from this source is

$$N_{background}(Drell - Yan \rightarrow e^+e^-) < 10^{-3}. \qquad (3.15)$$

5. $t\bar{t} \rightarrow e^+e^-$

   The mass of the top quark and the production cross section of $t\bar{t}$ pair are yet to be measured unambiguously. The background from $t\bar{t}$ is estimated a the top quark mass of 160, 170 and 180 GeV/c^2 using theoretical predictions of the cross sections. Then, an average of the results from the three top quark masses is quoted as the background from $t\bar{t}$ production.

$$N_{background}(t\bar{t} \rightarrow e^+e^-) = 0.028 \pm 0.007(\text{stat}) \pm 0.012(\text{syst}). \qquad (3.16)$$

   The main contribution to the systematic error is due to the averaging method. The systematic error also includes the luminosity uncertainty and the cross section uncertainty.

- Fake Background

  The fake background which contains both W+jet and QCD-multijet events is estimated in the following steps:

  1. Two sub-samples of data are derived from the full data set of the ELE-2-HIGH trigger. The first one is similar to our data sample and satisfies the standard electron-ID cuts. The events of the second sample, which is called the *fake* sample, must have at least one *bad* electron which has $\chi^2_H > 200$ and $Isolation > 0.15$. Figure 3.9 shows the missing E_T distributions of both samples.

2. A normalization factor (F) of the fake sample relative to the good sample is calculated using the numbers of events with $\not{E}_T < 15\text{GeV}$.
3. All the event selection cuts are applied to the fake sample and the number of events (N) which survive is counted.
4. The fake background is estimated to be

$$\begin{aligned} N_{background}(fake) &= F \times N \\ &= (0.038 \pm 0.003) \times (4 \pm 2) \\ &= 0.152 \pm 0.012(\text{stat}) \pm 0.076(\text{syst}). \end{aligned} \tag{3.17}$$

3.4.5 Summary of $W^+W^- \rightarrow e^+e^-$

The result for $W^+W^- \rightarrow e^+e^-$ analysis is summarized in the Table 3.6.

ϵ	0.094 ± 0.008
$N_{expected}(W^+W^- \rightarrow e^+e^-)$	$0.152 \pm 0.013(\text{stat}) \pm 0.024(\text{syst})$
$N_{background}$	$0.222 \pm 0.020(\text{stat}) \pm 0.080(\text{syst})$
N_{signal}	1

Table 3.6: Summary of $W^+W^- \rightarrow e^+e^-$ analysis.

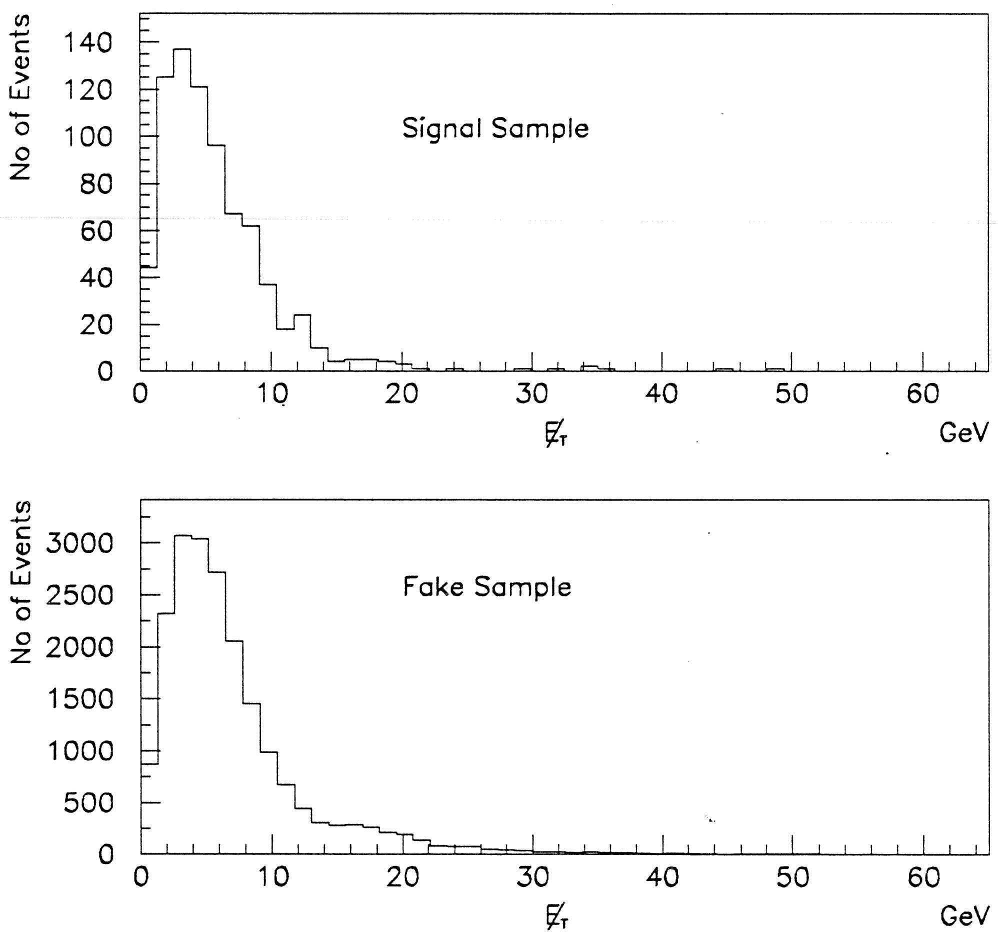

Figure 3.9: The $\not{E}_T$ distributions for *good* e^+e^- events and *fake* e^+e^- events.

3.5 Search for $W^+W^- \rightarrow e^{\pm} + \mu^{\mp} + X$

3.5.1 Luminosity, Trigger and Data Sample

The data set taken with the MU-ELE trigger is used for the $e^{\pm}\mu^{\mp}$ mode analysis. The trigger requires at least one EM tower with E_T greater than 7 GeV and a muon with $|\eta_{\mu}| < 1.7$ in level 1. In level 2 it is required that there be an EM cluster with E_T greater than 7 GeV and a muon with $p_T^{\mu} > 5$GeV. The initial number of events after cleaning for bad runs and noisy cells is 713 with $\int \mathcal{L}dt = 13.5 \pm 1.6 pb^{-1}$.

3.5.2 Event Selection

The following cuts are imposed to select candidate events:

- $E_T^e > 20$ GeV and $p_T^{\mu} > 15$ GeV
- $\not\!\!E_T \geq 20$ GeV
- For $\Delta\phi(p_T^{\mu}, \not\!\!E_T) < 20^o$ or $\Delta\phi(p_T^{\mu}, \not\!\!E_T) > 160^o$, $\not\!\!E_T \geq 50$ GeV

  where $\Delta\phi(p_T^{\mu}, \not\!\!E_T)$ is the angle between the muon and missing energy. This cut is similar to the e^+e^- channel and applied to remove $Z \rightarrow \tau^+\tau^- \rightarrow e^{\pm}\mu^{\mp}$. Figure 3.10 shows the 2-dimensional distributions of $\Delta\phi(p_T^{\mu}, \not\!\!E_T)$ vs $\not\!\!E_T$ for W pair production events with the SM couplings (generated with PYTHIA-DØGEANT), $Z \rightarrow \tau^+\tau^- \rightarrow e^{\pm}\mu^{\mp}$ (PYTHIA-DØGEANT), and W pair with the non-SM couplings (Zeppenfeld - DØ-FAST); $\Delta\kappa = 2$ and $\lambda = 0$.
- $|\vec{E_T}^{had}| \leq 40$GeV

  The $\vec{E_T}^{had}$ defined as the

$$\vec{E_T}^{had} = -(\vec{E_T}^{e} + \vec{E_T}^{\mu} + \vec{\not\!\!E_T}).$$

This cut is applied to reduce the background from $t\bar{t}$ production which is expected to have jet activity associated with it. Figure 3.11 shows the distributions of the $|\vec{E_T}^{had}|$ for the W pair events with the SM couplings (PYTHIA-DØGEANT), and $t\bar{t}$ events with $m_{top} = 170$ GeV/c^2 (PYTHIA-DØGEANT).

The result of the event selection on the data sample is listed in Table 3.7. No event survives after these cuts.

Event Selection Cut	Number of Events
Trigger+ID	17
$E_T^e \geq 20$ GeV	9
$p_T^\mu \geq 15$ GeV	6
$\not{E}_T \geq$ GeV	1
$\Delta\phi(p_T^\mu, \not{E}_T)$ cut	1
$\vec{E_T}^{had} \leq 40$ GeV	0

Table 3.7: The numbers of events after event selection cuts for $e^\pm\mu^\mp$ events.

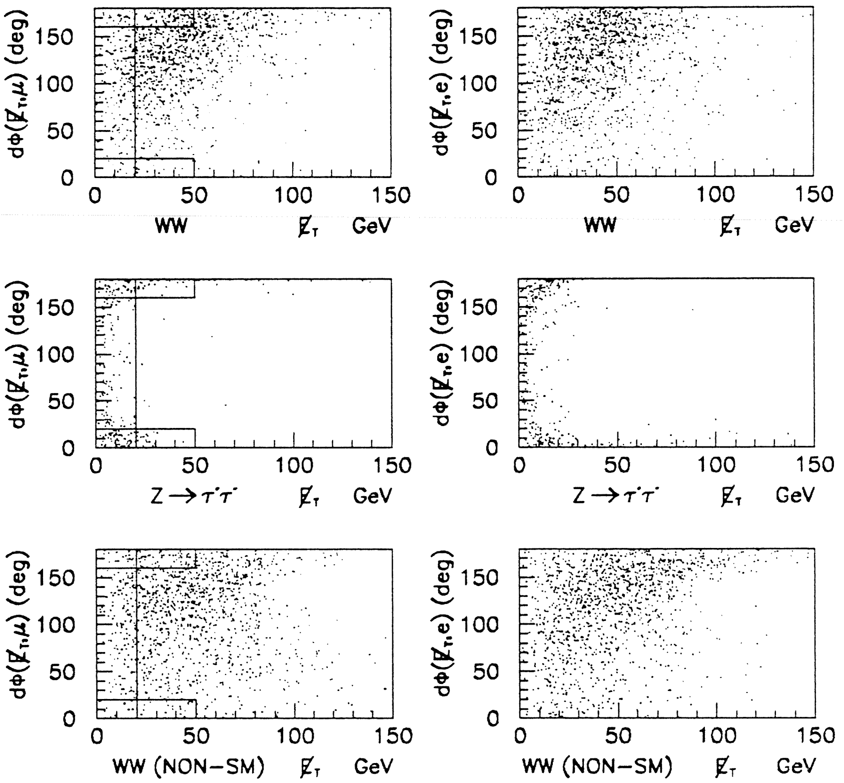

Figure 3.10: The 2-dimensional distributions of $\Delta\phi(E_T^e, \not E_T)$ vs $\not E_T$ and $\Delta\phi(p_T^\mu, \not E_T)$ vs $\not E_T$ for W pair production events with the SM couplings (PYTHIA-D0GEANT), $Z \rightarrow \tau^+\tau^- \rightarrow e^\pm\mu^\mp$ events (PYTHIA-D0GEANT), and W pair events with the non-SM couplings (Zeppenfeld-D0FAST).

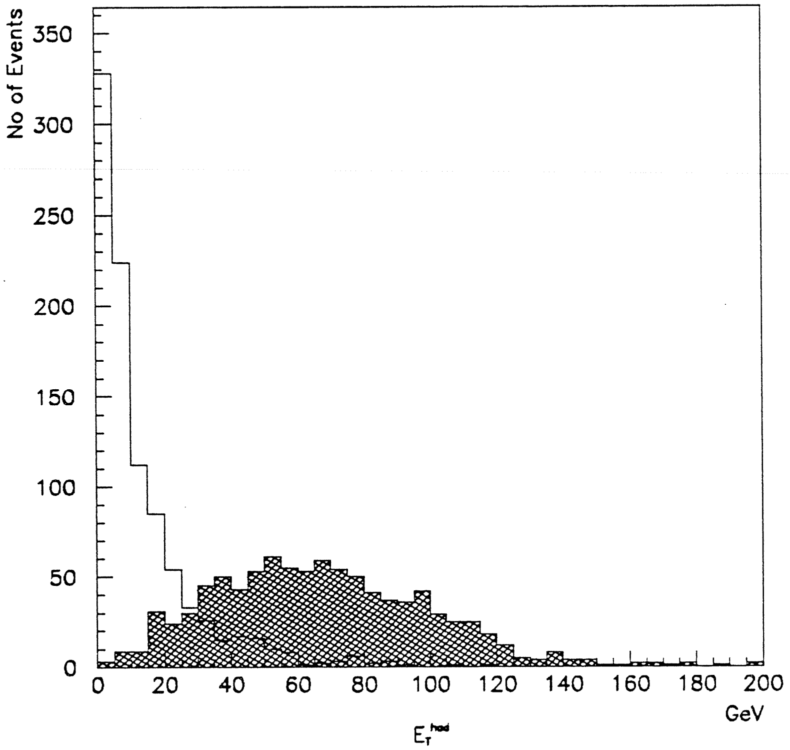

Figure 3.11: The distributions of the $|\vec{E}_T^{\,had}|$ for the $W^+W^- \rightarrow e^\pm\mu^\mp$ events with the SM couplings generated with PYTHIA-D0GEANT and $t\bar{t}$ events with $m_{top} = 170$ GeV/c^2 (hatched histogram).

3.5.3 Efficiency

The muon trigger efficiency is estimated using an unbiased sample of data [52]. The trigger efficiencies and the combined efficiencies for the trigger and muon and electron selections are listed in Tables 3.8 and 3.9.

Fiducial region	ϵ_{TRIG}
CC (EC) - CF	0.77 ± 0.05
CC (EC) - EF	0.36 ± 0.12

Table 3.8: The trigger efficiencies for $W^+W^- \rightarrow e^\pm\mu^\mp$ events.

The muon selection efficiencies are estimated using the W pair Monte Carlo events (generated with PYTHIA-DØGEANT). The MU-SMEAR package [42] is used to incorporate the measured efficiencies and resolutions of the muon chamber modules.

The detection efficiency is calculated by

$$\begin{aligned}\epsilon_{e\mu} &= \frac{1}{N^{MC}_{Gen}} \\ &\quad (\; N_{CC,CF} \; \epsilon^{CC,CF}_{ID+TRIG} \\ &\quad + \; N_{CC,EF} \; \epsilon^{CC,EF}_{ID+TRIG} \\ &\quad + \; N_{EC,CF} \; \epsilon^{EC,CF}_{ID+TRIG} \\ &\quad + \; N_{EC,EF} \; \epsilon^{EC,EF}_{ID+TRIG} \;),\end{aligned} \tag{3.18}$$

where $N^{MC}_{Gen} = 2500$ is the total number of generated events, and $N_{CC,CF} = 295$, $N_{CC,EF} = 117$, $N_{EC,CF} = 72$, and $N_{EC,EF} = 43$ are the numbers of events that

Fiducial region	$\epsilon_{ID+TRIG}$	Acceptance
CC - CF	0.43 ± 0.08	0.158 ± 0.009
CC - EF	0.21 ± 0.14	0.041 ± 0.004
EC - CF	0.30 ± 0.09	0.058 ± 0.005
EC - EF	0.15 ± 0.15	0.020 ± 0.003

Table 3.9: The combined efficiencies of trigger, electron and muon selections, and acceptance for $W^+W^- \rightarrow e^\pm\mu^\mp$ events.

survive all the cuts in the separate fiducial regions. The overall efficiency is

$$\epsilon_{e\mu} = 0.092 \pm 0.014, \tag{3.19}$$

where the error indicates uncertainties due to the trigger, the muon and electron identification, and the acceptance. The number of expected signal events is

$$N^{SM}_{expected}(W^+W^- \rightarrow e^\pm\mu^\mp) = 0.290 \pm 0.028(\text{stat}) \pm 0.045(\text{syst}). \tag{3.20}$$

The cross section ($\sigma \cdot Br(W^+W^- \rightarrow e^\pm\mu^\pm) = 0.24 \pm 0.02$ pb) and luminosity uncertainties are taken into account in the systematic uncertainty.

3.5.4 Background

Similar to the e^+e^- mode, there are both physics and fake backgrounds for $W^+W^- \rightarrow e^\pm\mu^\mp$ events. The physics background consists of $Z \rightarrow \tau^+\tau^- \rightarrow e^\pm\mu^\mp$,

$W^\pm\gamma \rightarrow \mu^\pm\gamma$ (where the γ is mis-identified as an electron), $b\bar{b} \rightarrow e^\pm\mu^\mp$, and $t\bar{t} \rightarrow e^\pm\mu^\mp$ processes. The fake background for this mode is an electron or a muon with a jet which is mis-identified as a muon or an electron.

- Physics Background

  1. $Z \rightarrow \tau^+\tau^- \rightarrow e^\pm\mu^\mp$

     4000 $Z \rightarrow \tau^+\tau^- \rightarrow e^\pm\mu^\mp$ events (PYTHIA-DØGEANT-DØRECO11.19) are used to estimate this background. The number of background events from this source is

     $$N_{background}(Z \rightarrow \tau^+\tau^-) = 0.114 \pm 0.049(\text{stat}) \pm 0.018(\text{syst}). \quad (3.21)$$

     The cross section ($\sigma \cdot Br = 12.3 \pm 1.2$ pb) and luminosity uncertainties are taken into account in the systematic uncertainty.

  2. $W^\pm\gamma \rightarrow \mu^\pm\gamma(\gamma \rightarrow e^\mp)$

     2500 $W^\pm\gamma$ events are generated with PYTHIA-DØGEANT and reconstructed with DØRECO11.19. The expected number of events from this source is

     $$N_{background}(W^\pm\gamma \rightarrow \mu^\pm\gamma) = 0.041 \pm 0.007(\text{stat}) \pm 0.030(\text{syst}). \quad (3.22)$$

     The systematic uncertainty includes the cross section and luminosity uncertainties.

  3. $b\bar{b} \rightarrow e^\pm\mu^\mp$

     2000 $b\bar{b}$ events are generated with ISAJET-DØGEANT and reconstructed with DØRECO11.19. The total number of background events from this source is

$$N_{background}(b\bar{b} \rightarrow e^{\pm}\mu^{\mp}) < 10^{-3}. \tag{3.23}$$

4. $t\bar{t} \rightarrow e^{\pm}\mu^{\mp}$

   The same method as for the e^+e^- mode is used for this mode as well.

$$N_{background}(t\bar{t} \rightarrow e^{\pm}\mu^{\mp}) = 0.035 \pm 0.005(\text{stat}) \pm 0.018(\text{syst}). \tag{3.24}$$

   The main contribution in systematic error is due to the averaging method. The systematic error also includes the luminosity uncertainty and the cross section uncertainty.

- Fake Background

  1. Isolated Muon from Jet

     This background is estimated using the probability of an isolated muon coming from a π/K decay in a jet. This background is estimated to be

$$N_{background}(Jet \rightarrow Fake\,\mu) < 10^{-4}. \tag{3.25}$$

  2. Jet Mis-identified as an Electron

     The inclusive $W^{\pm} \rightarrow \mu^{\pm}\nu$ data is used to estimate this background. Each jet in an event is treated as an electron and the event selection cuts are applied. Those events which survive the cuts are recorded and weighted by the appropriate probability of mis-identifying the jet as an electron. The initial number of events is 12881. The data sample with MU-MAX trigger is used which required a muon with $p_T^{\mu} > 15$GeV instead of MU-ELE. Since a different trigger is used, correction factors are calculated for different fiducial regions [53]:

$$\begin{aligned} F^{CF}_{scale} &= 2.02 \pm 0.15 \\ F^{EF}_{scale} &= 3.06 \pm 0.64 \end{aligned}$$

The correction factors come from differences between MU-ELE and MU-MAX triggers. First $p_T^\mu > 15$ GeV/c is required in the event selection. In level 2 MU-ELE trigger, the threshold for p_T^μ is 5 GeV/c. The MU-MAX trigger is implemented with the threshold of 15 GeV/c and is not fully efficient at 15 GeV/c. This inefficiency is calculated using data [53]:

$$\begin{aligned} F^{CF}_{threshold} &= (73 \pm 6)\% \\ F^{EF}_{threshold} &= 99\% \end{aligned}$$

Second, the MU-MAX trigger is prescaled whereas MU-ELE trigger is not. The effect of this prescaling is studied using both data and Monte Carlo and calculated as [53]:

$$\begin{aligned} F^{CF}_{prescale} &= 1.47 \pm 0.03 \\ F^{EF}_{prescale} &= 3.06 \pm 0.64 \end{aligned}$$

The correction factors are obtained by $F_{scale} = F_{prescale}/F_{threshold}$. The number of background events is calculated by

$$\begin{aligned} N_{background}(Jet \to Fake\, e) &= F^{CF}_{scale}(N^{jetCC}_{CF} P^{jetCC}_{fake} \\ &+ N^{jetEC}_{CF} P^{jetEC}_{fake}) \\ &+ F^{EF}_{scale}(N^{jetCC}_{EF} P^{jetCC}_{fake} \\ &+ N^{jetEC}_{EF} P^{jetEC}_{fake}) \end{aligned} \tag{3.26}$$

Where $N^{jetCC}_{CF} = 148$ is the number of events in which a muon is in the CF and a jet in the CC, $N^{jetEC}_{CF} = 58$ a jet in the EC and likewise for N^{jetCC}_{EF} and N^{jetEC}_{EF} in which a muon is in the EF. No events left in the EF region. P^{jetCC}_{fake}, and P^{jetEC}_{fake} are the probability of mis-identifying a jet as an electron in the CC, and EC region, respectively. [54]

$$\begin{aligned} P^{jetCC}_{fake} &= (0.9 \pm 0.4) \times 10^{-4} \\ P^{jetEC}_{fake} &= (4.0 \pm 1.0) \times 10^{-4} \end{aligned} \tag{3.27}$$

The fake background from this source is calculated to be

$$N_{background}(Jet \to Fake\, e) = 0.074 \pm 0.016(\text{stat}) \pm 0.074(\text{syst}). \tag{3.28}$$

The systematic error includes the uncertainties on the correction factors and the probability of mis-identifying a jet as an electron.

3.5.5 Summary of $W^+W^- \to e^\pm\mu^\mp$

The analysis for $W^+W^- \to e^\pm\mu^\mp$ is summarized in Table 3.10.

ϵ	0.092 ± 0.010
$N_{expected}(W^+W^- \to e^{\pm}\mu^{\mp})$	$0.290 \pm 0.028(\text{stat}) \pm 0.045(\text{syst})$
$N_{background}$	$0.264 \pm 0.052(\text{stat}) \pm 0.084(\text{syst})$
N_{signal}	0

Table 3.10: Summary of $W^+W^- \to e^{\pm}\mu^{\mp}$ analysis.

3.6 Search for $W^+W^- \to \mu^+ + \mu^- + X$

3.6.1 Luminosity, Trigger and Data Sample

A full data set taken during period (1992–1993) is used in the $\mu^+\mu^-$ mode analysis [55]. The luminosity for this data set is estimated to be $\int \mathcal{L}dt = 11.8 \pm 1.4 pb^{-1}$. In level 1 and 2 triggers, one muon is required to have $p_T^{\mu} > 15$GeV/c in $|\eta| < 1.7$.

3.6.2 Event Selection

The following cuts are applied to candidate events with two isolated muons:

- $p_T^{\mu 1} \geq 20$GeV/c and $p_T^{\mu 2} \geq 15$GeV/c

  where $\mu 1$ stands for a muon with higher p_T and $\mu 2$ for lower p_T.

- $E_T^{\eta} \geq 30$GeV/c

  The E_T^{η} is defined as the projection of $\vec{\not{E}}_T$ onto the bi-sector of the decay angles of two muons. Since the angle of muons are more precisely measured than their momenta, E_T^{η} is used rather than $\not{E}_T$.

- $\Delta\phi(p_T^{\mu 1}, \not{E}_T\ ) < 170^o$

  where $\Delta\phi(p_T^{\mu 1}, \not{E}_T\ )$ is the angle between the muon with higher p_T and missing energy. This cut is imposed to reduce $Z \rightarrow \tau^+\tau^- \rightarrow \mu^+\mu^-$ events, and $Z \rightarrow \mu^+\mu^-$ events with mis-measured muon momenta. Figure 3.12 shows the distributions of the E_T^{η} vs $\not{E}_T$ for W pair production (PYTHIA-DØGEANT), Z (PYTHIA-DØGEANT) and $t\bar{t}$ with $m_{top} = 160$ GeV/c^2 (PYTHIA-DØGEANT) events.

- $|\vec{E_T}^{had}| \leq 40\mathrm{GeV}$

  where $\vec{E}_T^{had}$ is defined as

  $$\vec{E}_T^{had} = -(\vec{E_T}^{\mu 1} + \vec{E_T}^{\mu 2} + \vec{\not{E}_T}\ )$$

  The same cut as in the other two channels is used to reduce the background from $t\bar{t}$ production which is expected to have jet activity associated with it. Figure 3.13 shows the distributions of the $|\vec{E_T}^{had}|$ for the W pair events with the SM couplings (PYTHIA-DØGEANT), and $t\bar{t}$ events with $m_{top} = 160$ GeV/c^2 (PYTHIA- DØGEANT).

After these cuts, no event survives. Table 3.11 shows the breakdown of the numbers of events after each cut.

Event Selection Cut	Number of Events
Trigger+ID	102
$p_T^{\mu 1} \geq 20\mathrm{GeV/c}$	102
$p_T^{\mu 2} \geq 15\mathrm{GeV/c}$	88
$E_T^{\eta} \geq 30\mathrm{GeV}$	0
$\Delta\phi(p_T^{\mu 1}, \not\!\!E_T) < 170^{o}$	0
$\lvert \vec{E_T}^{had} \rvert \leq 40\mathrm{GeV}$	0

Table 3.11: The numbers of events after event selection cuts for $\mu^+\mu^-$ events

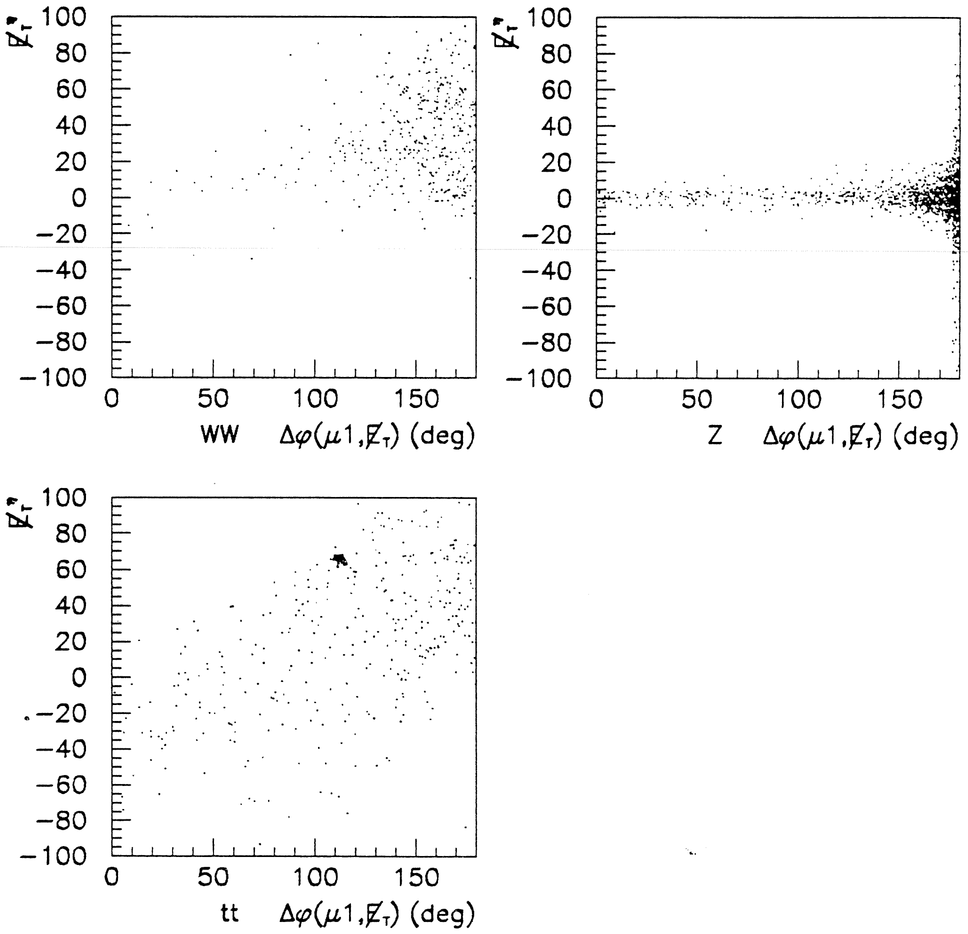

Figure 3.12: The distributions of the E_T^η vs $\Delta\phi(\mu 1, \not{E}_T)$ for W pair production, Z and $t\bar{t}$ with $m_{top} = 160$ GeV/c^2 (PYTHIA-DØGEANT) events.

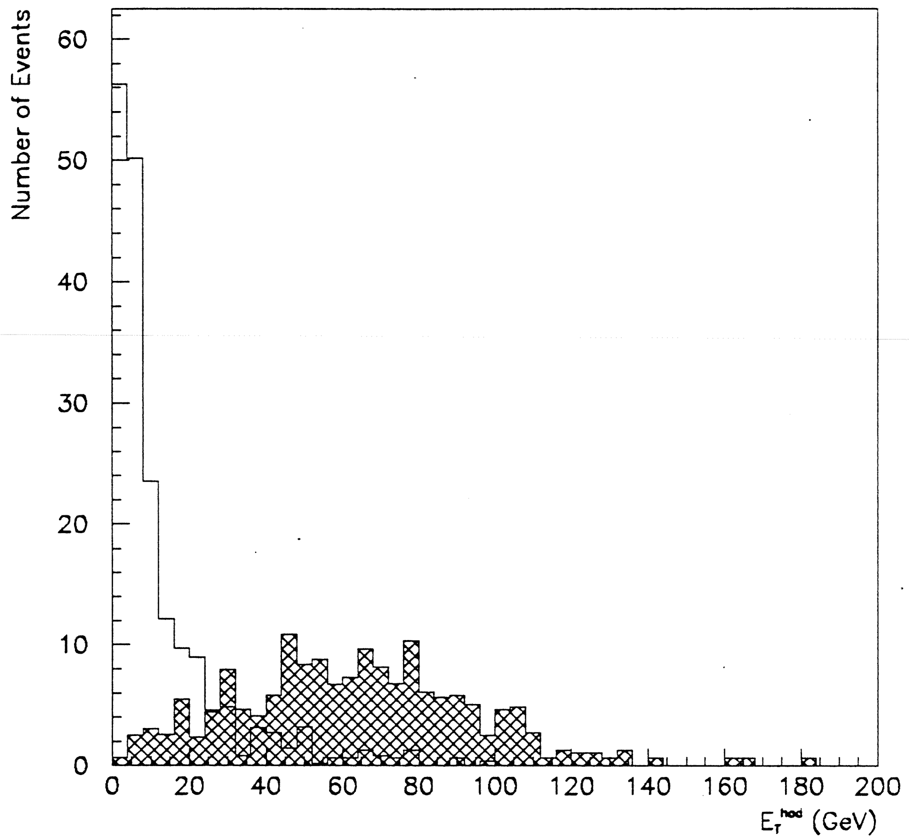

Figure 3.13: The distributions of the $|\vec{E_T}^{had}|$ for the $W^+W^- \rightarrow \mu^+\mu^-$ events with the SM couplings generated with PYTHIA-D0GEANT and $t\bar{t}$ events with $m_{top} = 160$ GeV/c^2 PYTHIA-D0GEANT (hatched histogram).

3.6.3 Efficiency

The trigger efficiencies are studied in [51, 56]. The trigger efficiencies are listed in Table 3.12.

Efficiency	Pre-shutdown	Post-shutdown	Luminosity weighted average
ϵ_{trig}^{CF-CF}	0.60 ± 0.08	0.67 ± 0.04	0.64 ± 0.04
ϵ_{trig}^{CF-EF}	0.34 ± 0.04	0.45 ± 0.03	0.41 ± 0.02
ϵ_{trig}^{EF-EF}	0.12 ± 0.04	0.21 ± 0.05	0.17 ± 0.03

Table 3.12: The trigger efficiencies for $W^+W^- \to \mu^+\mu^-$ events.

The detection efficiency is estimated from a Monte Carlo study and the trigger efficiencies. The same particle selection requirements and event selection cuts as data are applied to the $W^+W^- \to \mu^+\mu^-$ events (PYTHIA-D0GEANT). The number of events survived in each fiducial region is recorded as $N_{CF,CF}$, $N_{CF,EF}$ and $N_{EF,EF}$. The efficiency is calculated as

$$\epsilon_{\mu\mu} = \frac{1}{N_{Gen}^{MC}} \left(N_{CF,CF}\ \epsilon_{trig}^{CF,CF} + N_{CF,EF}\ \epsilon_{trig}^{CF,EF} + N_{EF,EF}\ \epsilon_{trig}^{EF,EF}\right), \quad (3.29)$$

where N_{Gen}^{MC} is the total number of generated events. From 2267 $W^+W^- \to \mu^+\mu^-$ events (PYTHIA-D0GEANT- D0RECO11.19), the following events survive all the cuts: $N_{CF,CF} = 81$, $N_{CF,EF} = 48$, and $N_{EF,EF} = 13$. The overall efficiency is estimated to be

$$\epsilon_{\mu\mu} = 0.033 \pm 0.003. \quad (3.30)$$

The uncertainty on the overall efficiency includes the uncertainties due to trigger efficiency, muon identifications, and acceptance. Table 3.13 shows the total efficiency in each fiducial region. The number of expected signal events with the estimated luminosity of $\int \mathcal{L}dt = 11.8 \pm 1.4pb^{-1}$ is calculated as

$$N^{SM}_{expected}(W^+W^- \rightarrow \mu^+\mu^-) \;=\; 0.046 \pm 0.004(\text{stat}) \pm 0.007(\text{syst}). \qquad (3.31)$$

The systematic error includes the uncertainties on the luminosity and cross section; $\sigma \cdot Br(W^+W^- \rightarrow \mu^+\mu^-) = 0.12 \pm 0.01$ pb.

Fiducial region	Efficiency
CF - CF	0.036 ± 0.004
CF - EF	0.021 ± 0.003
EF - EF	0.006 ± 0.002

Table 3.13: The overall detection efficiency for $W^+W^- \rightarrow \mu^+\mu^-$ events.

3.6.4 Background

There are two types of background, *physics* background and *fake* background, that compete with the $W^+W^- \rightarrow \mu^+\mu^-$ process, as in the other two channels. Among several physics processes that have a similar event structure to W pair events, only $Z \rightarrow \mu^+\mu^-$ and $t\bar{t} \rightarrow \mu^+\mu^-$ processes contribute significantly to the background in this channel. On the contrary to e^+e^- and $e^\pm\mu^\mp$ channels, the fake background in this channel is negligible.

- Physics Background

1. $Z \rightarrow \mu^+\mu^-$

   The fast Z Monte Carlo (ZKIN) developed at DØ for $Z \rightarrow e^+e^-$ is modified to generate $Z \rightarrow \mu^+\mu^-$ events. From 100000 events generated with ZKIN Monte Carlo, 8 events survive all the cuts. Using $\sigma \cdot Br(Z \rightarrow \mu^+\mu^-) = (0.21 \pm 0.03)$ nb, the background from this source is estimated to be

   $$N_{background}(Z \rightarrow \mu^+\mu^-) = 0.066 \pm 0.023(stat) \pm 0.0012(syst). \quad (3.32)$$

   Uncertainties on the cross section and luminosity are taken into account as the systematic error.

2. $Z \rightarrow \tau^+\tau^- \rightarrow \mu^+\mu^-$

   $Z \rightarrow \tau^+\tau^- \rightarrow \mu^+\mu^-$ events are generated using PYTHIA-DØGEANT-DØRECO11.19. From 2000 generated events none of them survive. The background events from this source is estimated to be

   $$N_{background}(Z \rightarrow \tau^+\tau^-) < 10^{-3}. \quad (3.33)$$

3. $t\bar{t} \rightarrow \mu^+\mu^-$

   The background from $t\bar{t}$ production for the top quark mass of 160 GeV/c^2 is estimated using the theoretical prediction of the cross section.

   $$N_{background}(t\bar{t} \rightarrow \mu^+\mu^-) = 0.009 \pm 0.002(stat) \pm 0.002(syst). \quad (3.34)$$

Uncertainties on the cross section and luminosity are taken into account as the systematic error.

3.6.5 Summary of $W^+W^- \to \mu^+\mu^-$

The analysis for $W^+W^- \to \mu^+\mu^-$ is summarized in Table 3.14.

ϵ	0.033 ± 0.003
$N_{expected}(W^+W^- \to \mu^+\mu^-)$	$0.046 \pm 0.004(\text{stat}) \pm 0.007(\text{syst})$
$N_{background}$	$0.075 \pm 0.023(\text{stat}) \pm 0.012(\text{syst})$
N_{signal}	0

Table 3.14: Summary of $W^+W^- \to \mu^+\mu^-$ analysis.

3.7 Limit on the Cross Section of the W Pair Production Process

A search for W pair production events in the three dilepton channels, e^+e^-, $e^\pm\mu^\mp$, and $\mu^+\mu^-$, is performed. The upper limit cross section can be extracted by combining the results from these three channels into the following:

$$\sigma = \frac{\sum_i (N_i^{Observed} - N_i^{Background})}{\sum_i \epsilon_i \cdot (\int \mathcal{L}dt)_i \cdot Br_i} \tag{3.35}$$

where i indicates three dilepton channels, and $N_i^{Observed}$, $N_i^{Background}$, ϵ_i, $(\int \mathcal{L}dt)_i$, and Br_i are the number of observed signal events, the number of estimated background events, the detection efficiency, the total integrated luminosity, and the branching ratio, respectively. The upper limit cross section with 95% confidence level is calculated using Poisson distributions for the numbers of events and Gaussian errors for the detection efficiencies, estimated background, and luminosities [57]. The result is

$$\sigma^{95\%CL} = 91\ pb, \tag{3.36}$$

which is to be compared with the Standard Model calculation in the next to leading order:

$$\sigma^{SM} = 9.5 \pm 1.0\ pb. \tag{3.37}$$

3.8 Limits on the Trilinear Gauge Boson Couplings

The limits on the trilinear gauge boson couplings can be obtained using the 95% confidence level limit of the W pair production cross section. It is assumed that the cross section is a bilinear function of the coupling constants, λ and $\Delta\kappa$, and can be written as

$$\sigma \cdot \epsilon = a_0 + a_1 \cdot \Delta\kappa + a_2 \cdot \lambda + a_3 \cdot (\Delta\kappa)^2 + a_4 \cdot (\lambda)^2 + a_5 \cdot \Delta\kappa \cdot \lambda, \tag{3.38}$$

where $\Delta\kappa = \kappa - 1$. All the other couplings are set to zero. In the Standard Model, $\Delta\kappa$ and λ are both zero. The form factor for the coupling is given as [21]

$$\lambda(s) \rightarrow \frac{\lambda}{(1 + s/\Lambda^2)^2} \tag{3.39}$$

where Λ is the form factor. The functional form of equation (3.39) is motivated by the Lagrangian of the triple gauge boson interactions. This form is examined by looking at the curve of $\sigma \cdot \epsilon$ with $\Delta\kappa = 0$ and $\lambda = 0$ separately. Figure 3.14 shows these two curves. They are in good agreement with our assumption.

The detection efficiency and cross section are calculated using the DØ-FAST Monte Carlo with the structure function set MRSD-. Twenty five grid points in the $(\Delta\kappa, \lambda)$ plane are used and for each of the grid points 25000 W pair events are generated. The results are listed in table 3.15.

The $\sigma \cdot \epsilon(\Delta\kappa, \lambda)$ is fitted using the equation (3.39) which has six parameters and a 3-dimensional surface with a minimum at the SM values $(\Delta\kappa = 0, \lambda = 0)$ is obtained. χ^2 for the surface fit is $\chi^2/(DoF) = 0.5$. The intersection of this surface with the 95% CL limit of the cross section in the $(\Delta\kappa, \lambda)$ plane determines the limits on the coupling constants. Figure 3.15 shows the $\sigma(\Delta\kappa, \lambda)$ surface. Figure 3.16 shows the contour of the intersection. The obtained limits on the coupling constants are as follows:

$$-2.6 < \Delta\kappa < 2.8 \quad (\lambda = 0)$$

$$-2.2 < \lambda < 2.2 \quad (\Delta\kappa = 0)$$

The form factor scale Λ used in this analysis is $\Lambda = 900$ GeV. The limits on the coupling parameters $\Delta\kappa$ and λ depend on the value of Λ, since the non-SM cross section (with nonzero $\Delta\kappa$ and λ) and the detection efficiencies depend on Λ. The value of Λ is chosen so that the contour of measured coupling limits stays inside of the contour of unitarity constraint as in Figure 3.16. By increasing the Λ to 950 GeV as in Figure 3.17, the two contours cross each other, indicating that the unitarity constraint is more stringent than the experimental limits in some areas of the $(\Delta\kappa, \lambda)$ plane. On the other hand, decreasing the Λ to 500 GeV makes the unitarity constraint far less stringent than the experimental limits, as shown in Figure 3.18. Since the purpose of this measurement is to test the Standard Model (which corresponds to the case of $\Lambda = \infty$), the highest value of Λ is chosen with the condition that the experimental constraint is more stringent than the unitarity constraint.

The $WW\gamma$ coupling can be studied through $W\gamma$ production. Figure 3.19 shows the $(\Delta\kappa_\gamma, \lambda_\gamma)$ contour limit from the $W\gamma$ production at the DØ experiment [27]. The $(\Delta\kappa, \lambda)$ contour limit from W pair production also is shown in Figure 3.19. Both results are compatible. The reason why the limits from the W pair production are compatible with the $W\gamma$ limits, even though the $W\gamma$ cross section is 10 times higher than the W pair cross section, is the characteristic cancellation in the W pair production process, as discussed in Chapter 1.

$\Delta\kappa$	λ	$\sigma \cdot \epsilon$
0	0	0.037 ± 0.003

$\Delta\kappa$	λ	$\sigma \cdot \epsilon$	$\Delta\kappa$	λ	$\sigma \cdot \epsilon$
0	1	0.105± 0.008	1	0	0.069 ± 0.005
0	-1	0.108±0.008	-1	0	0.089 ± 0.007
0	2	0.309± 0.022	2	0	0.182 ± 0.013
0	-2	0.320±0.021	-2	0	0.222 ± 0.017
1	1	0.141 ± 0.010	-1	-1	0.0163 ± 0.013

$\Delta\kappa$	λ	$\sigma \cdot \epsilon$	$\Delta\kappa$	λ	$\sigma \cdot \epsilon$
1	-1	0.132 ± 0.010	-1	1	0.148 ± 0.011
1	2	0.354 ± 0.026	2	1	0.262 ± 0.020
1	-2	0.343 ± 0.024	-2	1	0.271 ± 0.019
2	1	0.262 ± 0.020	1	2	0.354 ± 0.026
2	-1	0.242 ± 0.018	-1	2	0.345 ± 0.025
2	2	0.489 ± 0.035	-2	-2	0.536 ± 0.038
2	-2	0.436 ± 0.033	-2	2	0.473 ± 0.033

Table 3.15: The $\sigma \cdot \epsilon(W^+W^- \rightarrow l^-l^+)$ (pb) as a function of $\Delta\kappa$ and λ, where $l = e$ *or* μ .

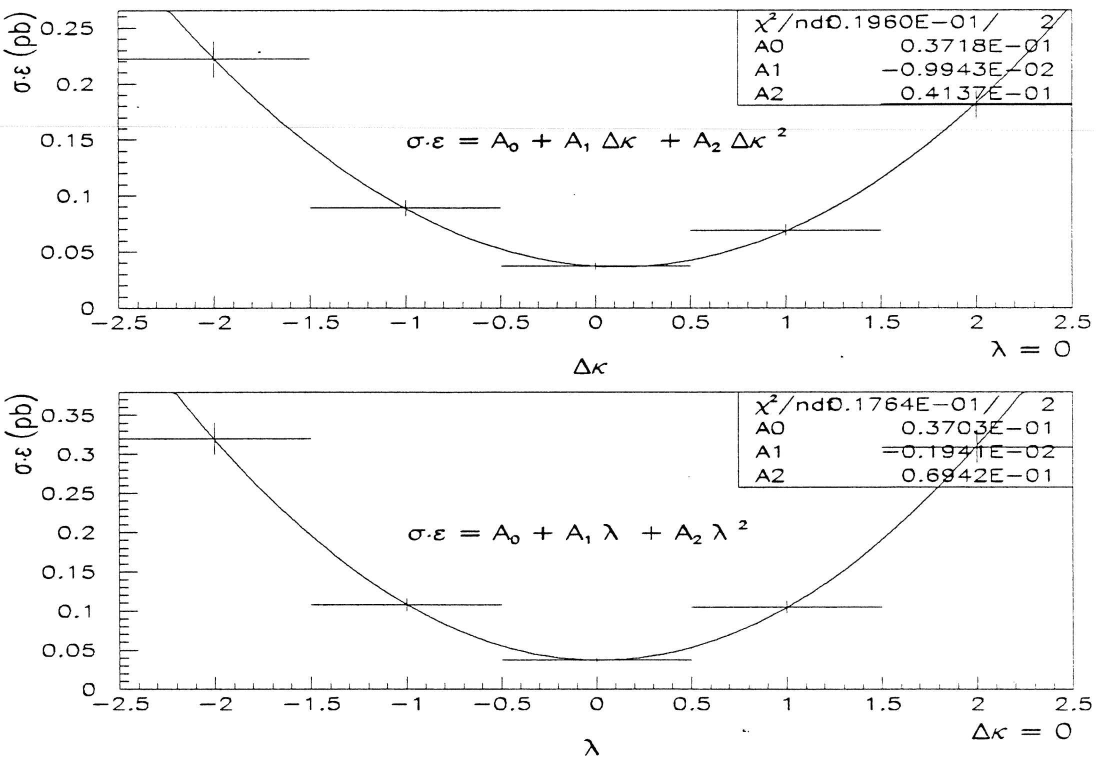

Figure 3.14: The $\sigma \cdot \epsilon$ as a function of $\Delta\kappa$ for $\lambda = 0$ and as a function of λ for $\Delta\kappa = 0$.

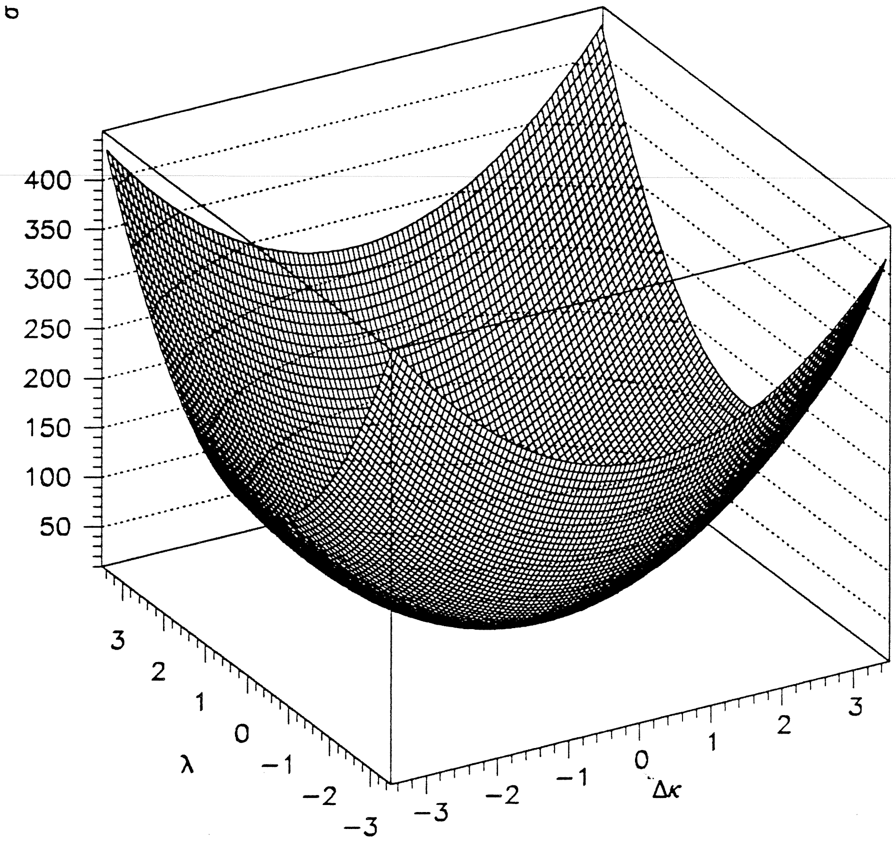

Figure 3.15: The surface plot of σ (pb) as a function of $\Delta\kappa$ and λ.

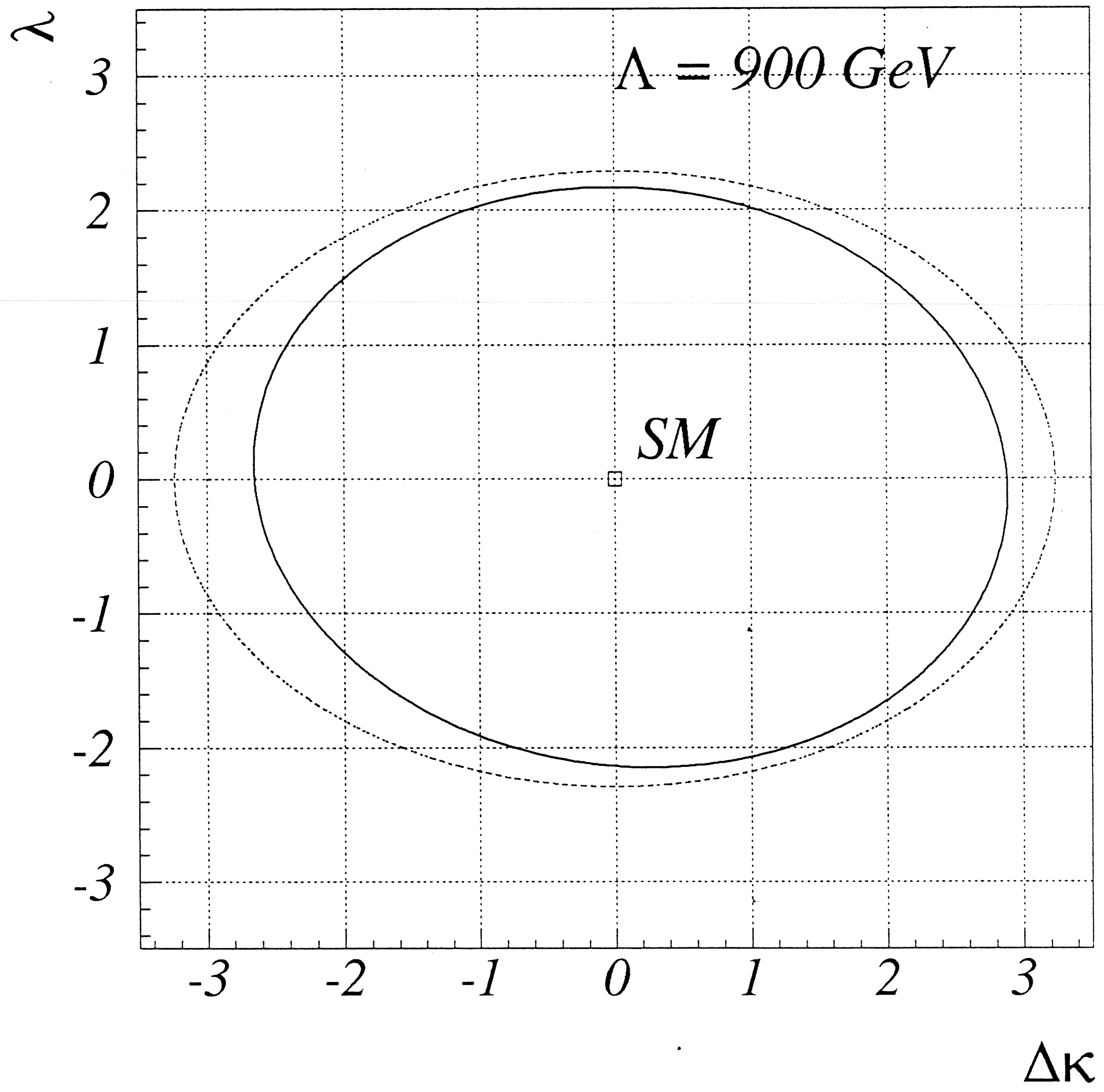

Figure 3.16: The contour limit on the trilinear gauge boson couplings of this analysis with the form factor scale $\Lambda = 900$ GeV. The solid line and dotted line correspond to the experimental limit and the unitarity constraint, respectively.

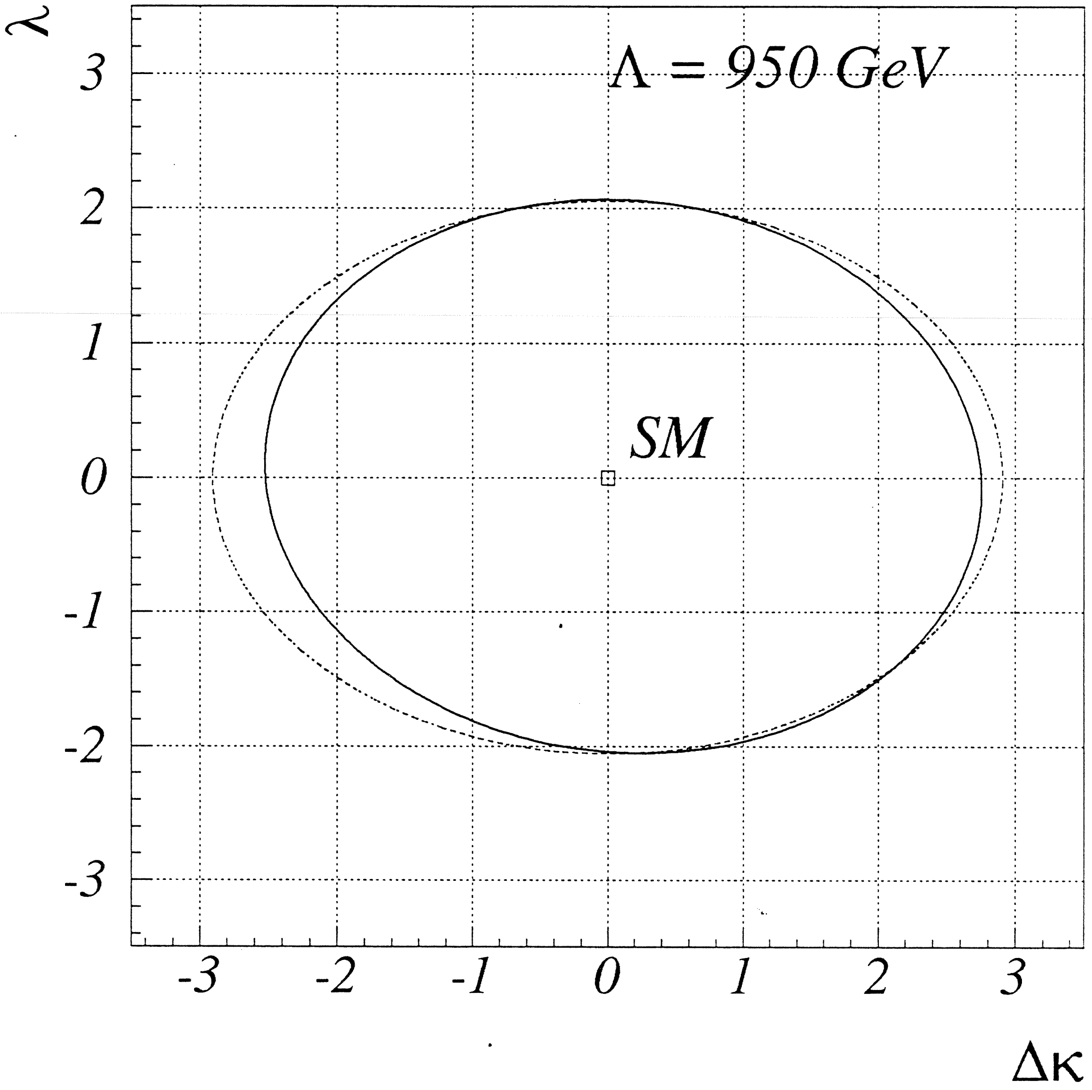

Figure 3.17: The contour limit on the trilinear gauge boson couplings with $\Lambda = 950$ GeV. The solid line and dotted line correspond to the experimental limit and the unitarity constraint, respectively.

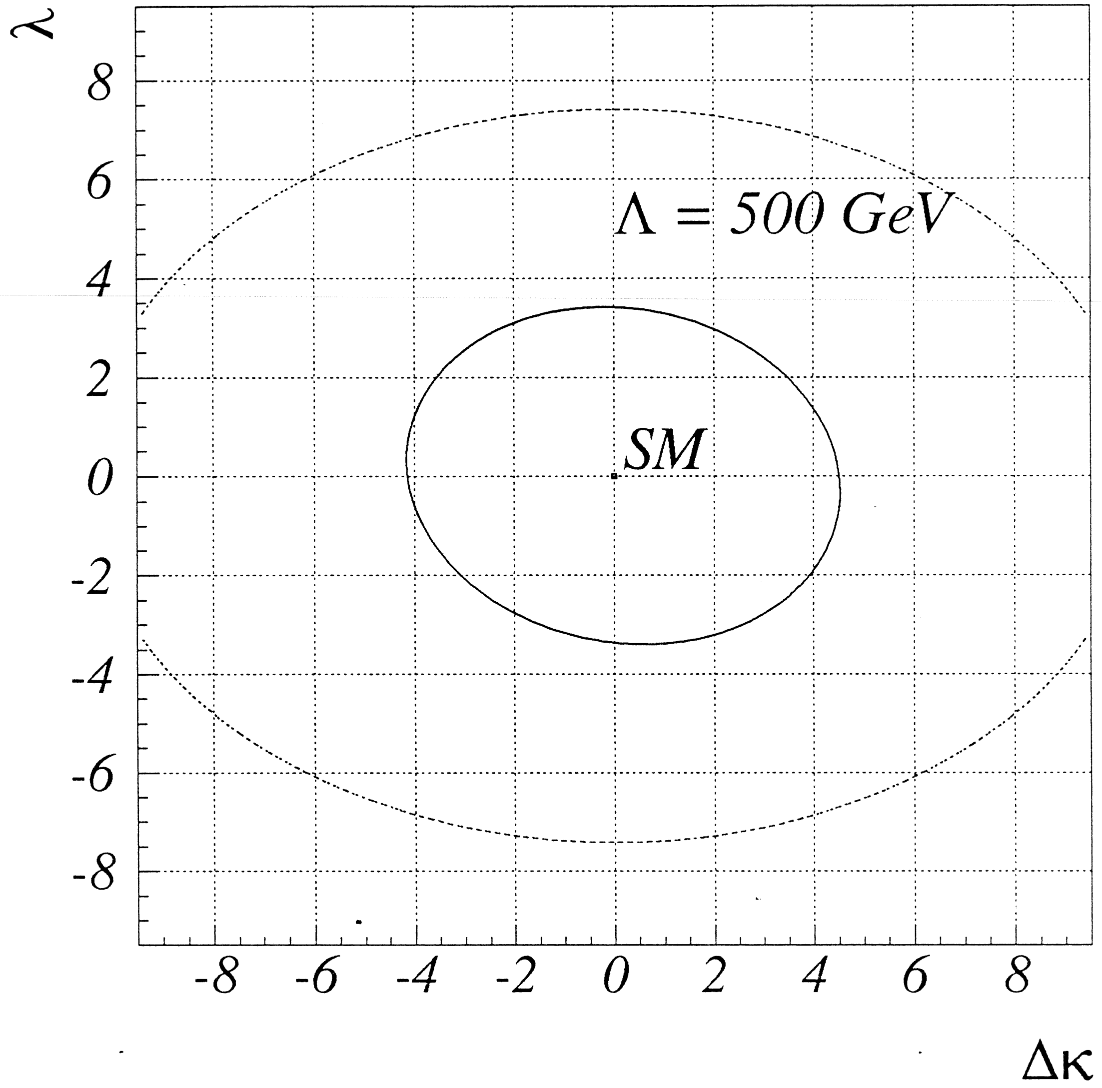

Figure 3.18: The contour limit on the trilinear gauge boson couplings with $\Lambda = 500$ GeV. The solid line and dotted line correspond to the experimental limit and the unitarity constraint, respectively.

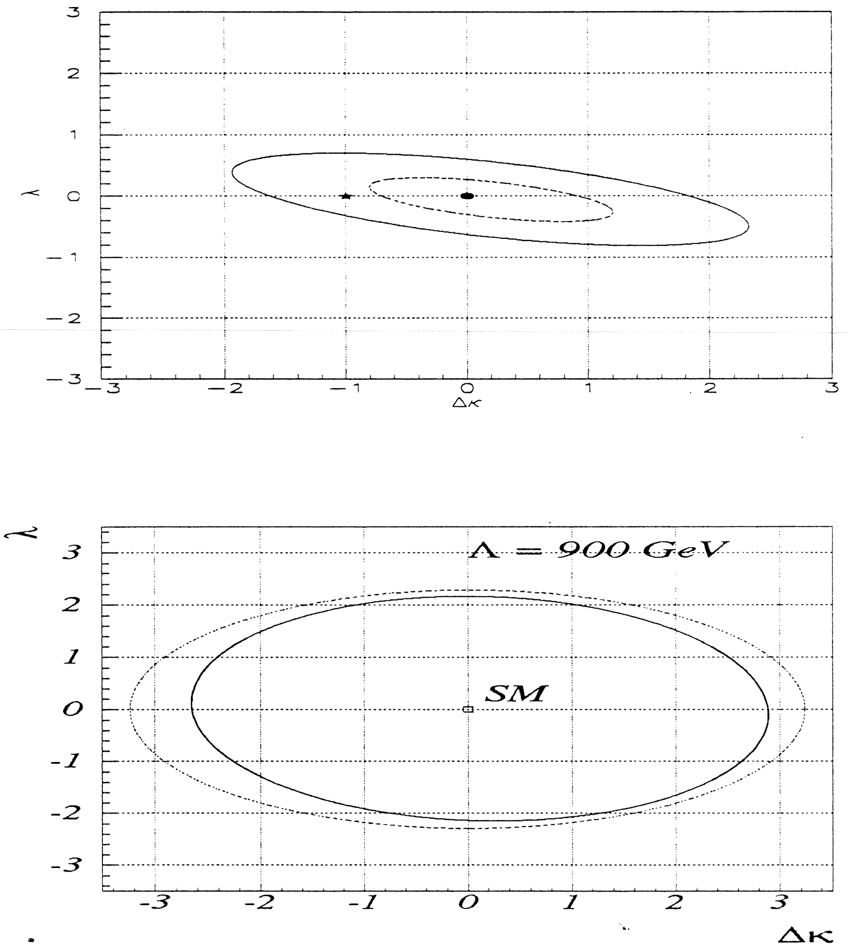

Figure 3.19: The contour limit on the trilinear gauge boson couplings from $W\gamma$ (top plot) and W pair (bottom plot) productions. In the top plot ($W\gamma$) the solid line and dotted line correspond to the 95 % CL and 68 % CL limit, respectively. In the bottom plot (W pair) the solid line and dotted line correspond to the experimental limit and the unitarity constraint, respectively.

Chapter 4

Conclusions

A search for W pair production events in the dilepton channels, e^+e^-, $e^\pm\mu^\mp$, and $\mu^+\mu^-$ in $p\bar{p}$ collisions at $\sqrt{s} = 1.8$ TeV has been performed. One event in the e^+e^- channel and 0 events in both of the $e^\pm\mu^\mp$ and $\mu^+\mu^-$ channels are observed. The expected numbers of signal events with the Standard Model couplings and background events after combining all the channels are $0.49 \pm 0.04 \pm 0.05$ and $0.57 \pm 0.04 \pm 0.10$, respectively. No serious deviation from the Standard Model is observed. The 95% CL limit of the W pair production cross section is calculated to be $\sigma^{95\%\ CL} = 91\ pb$. This cross section limits the range of possible γWW and ZWW coupling parameters to $-2.6 < \Delta\kappa < 2.8$ for $\lambda = 0$ and $-2.2 < \lambda < 2.2$ for $\Delta\kappa = 0$, assuming the coupling parameters for γWW and ZWW have the same strengths. This analysis provides a first test of the Standard Model W pair production process which is characterized by the delicate cancellations among the contributing diagrams which prevent the unitarity violation in the Standard Model.

The coupling limits will be significantly improved by the future experiments at the Tevatron with integrated luminosities greater than 1 fb^{-1}, and at LEP II as well as LHC at CERN [58]. Table 4.1 shows the expected results from these experiments.

The measurement of triple gauge boson couplings will be a crucial element of high energy experimental physics in the next 20 years.

	Tevatron ($p\bar{p}$)	LEP II (e^+e^-)	LHC (pp)
Energy	1.8 TeV	190 GeV	14 TeV
$\int L dt$ (fb^{-1})	10	0.5	100
Λ	1 TeV		3 TeV
$\Delta\kappa$ Coupling	$-0.12 < \Delta\kappa < 0.16$	$-0.13 < \Delta\kappa < 0.14$	$-0.08 < \Delta\kappa < 0.08$
λ Coupling	$-0.10 < \lambda < 0.11$	$-0.13 < \lambda < 0.14$	$-0.06 < \lambda < 0.06$

Table 4.1: The sensitivity of future Tevatron, LEP II, and LHC experiments.

Bibliography

[1] F. Hasert, et al. *Phys. Lett.*, **45B**:1, 1973.

[2] G. Arnison, et al. (UA1 Collaboration) *Phys. Lett.*, **122B**:1, 1983.

[3] P. Bagnaia, et al. (UA2 Collaboration) *Phys. Lett.*, **129B**:130, 1983.

[4] Particle Data Group, L. Montanet et al. *Phys. Rev. D*, **50**:1173, 1994.

[5] S. Abachi et al., Submitted to Phys. Rev. Lett.

[6] D.H. Perkins. *Introduction to High Energy Physics*, ADDISON-WESLEY, 1987.

[7] S. Glashow. *Nucl. Phys.*, **22**:579, 1961.

[8] S. Weinberg. *Phys. Rev. Lett.*, **19**:1264, 1967.

[9] P. Higgs. *Phys. Rev. Lett.*, **13**:508, 1964.

[10] J.R. Aitchison and A.J.G. Hey. *Gauge Theories in Particle Physics*, ADAM HILGER, 1989.

[11] M. Kobayashi and K. Maskawa. *Prog. Theo. Phys.*, **49**:652, 1975.

[12] R.W. Brown and K.O. Mikaelian. *Phys. Rev. D*, **19**:922, 1979.

[13] S. Willenbrock and D.Zeppenfeld. *Phys. Rev. D*, **37**:1775, 1988.

[14] C. Chang and S.C. Lee. *Phys. Rev. D*, **37**:101, 1988.

[15] K. Hagiwara, K. Hikasa, R.D. Peccei and D. Zeppenfeld. *Nucl. Phys.*, **B282**:253, 1987.

[16] K. Hagiwara, S. Ishihara , R. Szalapski and D. Zeppenfeld. *MAD/PH/737*, KEK preprint 92-214:22, 1993.

[17] K. Lane E. Eichten, I. Hinchliffe and C.Quigg. *Rev. Mod. Phys.*, **56**:579, 1984.

[18] V.D. Barger and R.J.N. Phillips. *Collider Physics*, ADDISON-WESLEY, 1987.

[19] K.O. Mikaelian R.W. Brown and D. Sahdev. *Phys. Rev. D*, **20**:1164, 1979.

[20] C. Quigg B.W. Lee and H.B. Thacker. *Phys. Rev. D*, **16**:1519, 1977.

[21] J. Woodside, K. Hagiwara and D. Zeppenfeld. *Phys. Rev. D*, **41**:2113, 1990.

[22] H. Plothow-Besch, PDFLIB v4.15, CERN Program Library, (unpublished) 1993.

[23] CDF Collaboration, F. Abe et al., submitted to Phys. Rev. Lett.

[24] A. Martin et al., *Phys. Lett.*, **B306**:145, 1993.

[25] UA2 Collaboration, J. Alitti et al., *Phys. Lett.*, **B277**:194, 1992.

[26] CDF Collaboration, F. Abe et al., submitted to Phys. Rev. Lett.

[27] DØ Collaboration, S. Abachi et al., submitted to Phys. Rev. Lett.

[28] H. Aihara, et al. DPF Report, (unpublished) 1995.

[29] M. Alam, et al. (CELO Collaboration) CLNS-94-1314 preprint, 1994.

[30] J. Thompson, Private Communication

[31] N. Amos, et al. *D0-Note*, 2031 Fermi National Laboratory, 1994, (unpublished).

[32] S. Abachi et al., *Nucl. Instr. Meth.*, **A324**:53, 1993.

[33] R. Fernow. *Introduction to Experimental Particle Physics*, Cambridge University Press, Cambridge, 1990

[34] J.H. Cochran. *Ph.D thesis*, State University of New York at Stony Brook, 1993, (unpublished)

[35] J. Yu. *Ph.D thesis*, State University of New York at Stony Brook, 1993, (unpublished)

[36] C. Gerber et al., *D0-Note*, 2140 Fermi National Laboratory, 1994, (unpublished)

[37] A. J. Milder. *Ph.D thesis*, University of Arizona, 1993, (unpublished)

[38] M. Paterno et al. *D0-Note*, 1782 Fermi National Laboratory, 1993, (unpublished)

[39] M. Narain and U. Heintz. *D0-Note*, 1814 Fermi National Laboratory, 1993, (unpublished)

[40] N. Denisenko. *D0-Note*, 1885 Fermi National Laboratory, 1993, (unpublished)

[41] F. Carminati et al., *GEANT Users Guide*, CERN Program Library, 1991 (unpublished).

[42] T. Diehl. MU-SMEAR Documentation, Fermi National Laboratory, 1994, (unpublished)

[43] T. Sjostrand. Pythia 5.6 manual. Theory Division, CERN, 1992. (unpublished)

[44] F. Paige and S. Protopopescu. BNL Report no. BNL38034, 1992. (unpublished)

[45] R. Field and R. Feynman. *Nucl. Phys.*, **B136**:1 , 1978.

[46] B. Anderson, et al. *Phys. Rep.*, **97**:33, 1983.

[47] P. Arnold and R. Kauffman. *ANL-HEP-PR-90-70*, 1990.

[48] M. Demarteau, Private Communication

[49] D. Zeppenfeld and U. Baur, Private Communication

[50] C. Gerber et al. *D0-Note*, 1985 Fermi National Laboratory, 1994, (unpublished)

[51] H. Johari et al. *D0-Note*, 2391 Fermi National Laboratory, 1994, (unpublished)

[52] D. Wood, Private Communication

[53] H. Aihara et al. *D0-Note*, 2000 Fermi National Laboratory, 1994, (unpublished)

[54] M. Kelly, et al. *D0-Note*, 2215 Fermi National Laboratory, 1994, (unpublished).

[55] T. Yasuda, Private Communication
(This part of analysis is done by T. Yasuda).

[56] C. Gerber et al. *D0-Note*, 2214 Fermi National Laboratory, 1994, (unpublished)

[57] R. Partridge. *D0-Note*, 1806 Fermi National Laboratory, 1993, (unpublished)

[58] H. Aihara et al. *FERMILAB-Pub-95/031*, 1995.